Multimodal Retinal Imaging via OCT Multi-Volume Averaging and Two Photon Excited Fluorescence

by

William Brian Newberry

Bachelor of Science, Simon Fraser University, 2020

Thesis Submitted in Partial Fulfillment of the
Requirements for the Degree of
Master of Applied Science

in the
School of Engineering Science
Faculty of Applied Sciences

SIMON FRASER UNIVERSITY
Fall 2022

Declaration of Committee

Name:	**William Brian Newberry**
Degree:	**Master of Applied Science**
Title:	**Multimodal Retinal Imaging via OCT Multi-Volume Averaging and Two Photon Excited Fluorescence**
Committee:	**Chair:** **Mirza Faisal Beg** Professor, Engineering Science
	Marinko V. Sarunic Supervisor Professor, Engineering Science
	Yifan Jian Committee Member Assistant Professor, Engineering Science
	Myeong Jin Ju Committee Member Assistant Professor, Engineering Science
	Pierre Lane Examiner Associate Professor, Engineering Science

Ethics Statement

The author, whose name appears on the title page of this work, has obtained, for the research described in this work, either:

a. human research ethics approval from the Simon Fraser University Office of Research Ethics

or

b. advance approval of the animal care protocol from the University Animal Care Committee of Simon Fraser University

or has conducted the research

c. as a co-investigator, collaborator, or research assistant in a research project approved in advance.

A copy of the approval letter has been filed with the Theses Office of the University Library at the time of submission of this thesis or project.

The original application for approval and letter of approval are filed with the relevant offices. Inquiries may be directed to those authorities.

Simon Fraser University Library
Burnaby, British Columbia, Canada

Update Spring 2016

Abstract

Advancements in optical imaging are needed to study vision robbing diseases. New technology can be developed using animal models, which can progress the understanding of both retinal function, and that of novel imaging methods. Fluorescence is a convenient source of contrast in the retina due to the relative ease of introducing extrinsic fluorophores, as well as its various opportunities for autofluorescence. two-photon excited fluorescence (TPEF) is a suitable modality of this, but its need for high incident powers arises concerns of damaging the retina. A pulsed laser coupled with high numerical aperture and adaptive optics aids to lower the required power, but sample motion remains an issue. In this thesis, I present on improvements made to a TPEF imaging system, as well as an algorithm that utilizes co-acquired optical coherence tomography (OCT) to aid in motion correction.

Keywords: Sensorless Adaptive Optics; Two-Photon Excited Fluorescence; Scanning Laser Ophthalmoscopy; Optical Coherence Tomography; Image Registration

To my parents, Charles and Melissa Newberry

Acknowledgements

I would like to acknowledge the continued support of my supervisor Dr. Marinko Sarunic. His passion for this field shows clearly throughout his research and his teaching, which has enabled me and many others to pursue exciting opportunities both in the lab and around the world. He has my utmost gratitude for supporting me through a time of significant hardship, and it has been an honour to learn from him.

While there are many to thank, I would like to especially extend my gratitude to Dr. Daniel Wahl for educating me on the many facets and subtleties of his imaging system which he developed alongside the research group.

I would also like to acknowledge the members of the SFU Biomedical Optics Research Group who through the years have collectively maintained both a productive research collaboration, as well as a fun social circle.

Lastly, I would like to thank my family, friends, and my wife Emily for supporting me throughout my academics.

Table of Contents

Declaration of Committee ii
Ethics Statement iii
Abstract iv
Dedication v
Acknowledgements vi
Table of Contents vii
List of Tables ix
List of Figures x
List of Acronyms xiii

Chapter 1. Introduction 1
1.1. Overview 1
1.2. The mouse eye 2
1.3. Imaging the mouse retina 5
1.4. Outline 7
1.5. Contributions 8

Chapter 2. Background on retinal imaging systems and adaptive optics 10
2.1. Scanning Laser Ophthalmoscopy 10
2.2. Optical Coherence Tomography 11
2.3. Fluorescence Imaging 12
2.4. Adaptive Optics for Ophthalmic Imaging 14
2.5. Multimodal Imaging for Non-Invasive Applications 16
2.6. Summary 17

Chapter 3. Wavefront sensorless adaptive optics TPEF for *in vivo* retinal imaging in mice 18
3.1. Introduction 18
3.2. Methods 19
3.2.1. Mouse Handling 19
3.2.2. Optical Design 20
3.2.3. Adaptive Optics Optimization 21
3.3. Results 22
3.3.1. Design considerations via Zemax Optic Studio 22
3.3.2. *In vivo* WSAO TPEF with increased numerical aperture 28
3.4. Discussion 30
3.5. Summary 31

Chapter 4. Multi-modal imaging for low-power TPEF imaging 33
4.1. Introduction 33
4.2. Methods 34
4.3. Results 40
4.3.1. AO and image registration for low power TPEF imaging 40

4.3.2. RPE imaging 45
4.4. Discussion 46

Chapter 5. Future work and conclusion 48
5.1. Technology Advancement 48
5.2. Fluorescent Lifetime Microscopy 48
5.3. Conclusion 49

References 50

List of Tables

Table 2.1. Zernike polynomials and names up to 14th index [23]. 15

List of Figures

Figure 1. 1. Schematic comparing mouse eye to human eye [4]. 3

Figure 1. 2. Histological image of retinal layers [6]. 4

Figure 1. 3. Diagram of the visual cycle between outer rod segments and the RPE [7]. 5

Figure 1. 4. Diagram demonstrating the function of Adaptive Optics [8]. 6

Figure 1. 5. Diagram demonstrating the function of a Shack-Hartmann Wavefront Sensor [9]....7

Figure 3. 1. Schematic of the SAO OCT and TPEF imaging system. The imaging system was constructed with a pellicle beam splitter (PeBS), variable focus lens (VFL), deformable mirror (DM), dichroic mirror (DcM), galvanometer-scanning mirrors (GM), emission filters (EF), photo-multiplier tube (PMT), dispersion compensation (DC), and the following lenses: L1=100 mm, L2=300 mm, L3=400 mm, L4=100 mm, L5=2x125 mm, L6=2x50 mm. The reference arm denoted as a dashed line [12]. ...20

Figure 3. 2. Schematic of the changes made to the TPEF detection path on the SAO OCT and TPEF imaging system. Dichroic mirror (DcM) was moved to between final relay lenses to avoid loss of signal when de-scanned by galvanometer mirrors (GM). Lenses shown are L5=2x125 mm, L6=2x50 mm to optically relay GM to mouse pupil, and PMT focusing lens 60 mm. 23

Figure 3. 3. A simulation of the forward path of the SAO OCT and TPEF imaging system using Zemax Optic Studio. A model mouse eye was used, where the anterior and posterior segments of the retina are shown with a $\pm 2o$ scan [Gardner et al mouse eye]. L1=100 mm, L2=300 mm, L3=400 mm, L4=100 mm, L5=2x100 mm, L6=50 mm. 24

Figure 3. 4. A simulation of the foci generated in the mouse retina under a $\pm 1o$ scan. Shown is a scan with a 0 diopter contribution from the VFL (a), 15 diopters (b), and 20 diopters after preceding the VFL a 200 mm focal length achromatic doublet (c). 25

Figure 3. 5. A chart from Zemax simulation displaying system aberrations under varying VFL curvatures ranging from 0 to 20 diopters. Data is displayed as Zernike coefficient versus Zernike index. 26

Figure 3. 6. A chart from Zemax simulation displaying system aberrations under varying VFL curvatures ranging from 0 to 20 diopters under influence of $\pm 2o$ scan via galvanometer mirrors. Data is displayed as Zernike coefficient versus Zernike index. 26

Figure 3. 7. A chart from Zemax simulation displaying aberrations present at the focal plane of a mouse imaging configuration. Results were taken for an on-axis beam for both a mouse eye square with the optical axis, and with a 3-degree rotation about the vertical axis. 27

Figure 3. 8. TPEF SLO images from a sample of lens tissue soaked with fluorescein, showing both a single frame (a), and an average of 200 frames (b). 28

Figure 3. 9. In *vivo* Two Photon Excited Fluorescence (TPEF) images of the nerve fibre layer (NFL) of a transgenic YFP-labelled mice taken before (left column) and after (right column) images guided Sensorless Adaptive Optics (SAO), with an objective lens numerical aperture (NA) of 0.25 (top row) and 0.40 (bottom row). Scale bars: 20 μm. 30

Figure 4. 1. Schematic of the SAO OCT and TPEF imaging system. The imaging system was constructed with pre-chirp pulse compressor, a pellicle beam splitter (PeBS), variable focus lens (VFL) preceded by 200mm lense (PL), deformable mirror (DM), dichroic mirror (DcM), galvanometer-scanning mirrors (GM), emission filters (EF), photo-multiplier tube (PMT), dispersion compensation (DC), and the following lenses: L1=100 mm, L2=300 mm, L3=400 mm, L4=100 mm, L5=2x125 mm, L6=2x50 mm. The reference arm denoted as a dashed line 35

Figure 4. 2. A comparison of OCT B-scans from 2 separate volumes acquired 6 seconds apart, where magenta shows the target frame, and green the reference. Left shows before cross-correlation based motion correction, and right after. 36

Figure 4. 3. A comparison of TPEF and OCT displacement fields between the target and reference frame (a), demonstrating their shared motion. Below are overlays of the corresponding frames where magenta shows the target frame, and green the reference, for both TPEF (b) and OCT (c). 38

Figure 4. 4. Averaged TPEF frames from fluorescent lens paper phantom showing an intensity line plot for each between the arrows (a), unregistered frames (b), frames registered via OCT reference (c), and frames registered via TPEF reference (d). 39

Figure 4. 5 Comparison of motion, between single frames of TPEF from *in vivo* images from a YFP labelled mouse (left), and fluorescein-soaked lens paper (right). Average motion in the former was ~8% of the FOV, and ~4% in the latter. 39

Figure 4. 6. (a) In *vivo* Two Photon Excited Fluorescence (TPEF) and Optical Coherence Tomography (OCT) *en face* images of the nerve fiber layer (NFL) of a transgenic YFP-labelled mouse taken at 0.4 NA, before and after image guided Sensorless Adaptive Optics (SAO). (b) Zernike coefficients applied to the deformable mirror. Scale bars: 20 μm. 41

Figure 4. 7. In *vivo* Two Photon Excited Fluorescence (TPEF) *en face* images of the nerve fiber layer (NFL) of a transgenic YFP-labelled mouse taken at 0.4 NA, with 1.3 mW incident laser power (left) and 0.625 mw (right). Scale bars: 20 μm. 42

Figure 4. 8. In *vivo* TPEF and OCT *en face* images of the nerve fiber layer (NFL) of a transgenic YFP-labelled mouse taken at 1.3 mW incident laser power and 0.4 NA. Shown is a single frame of TPEF and a maximum intensity projection of the same layer from the corresponding OCT volume (a), and then the average of 100 unregistered frames (b), frames registered via OCT reference (c), and frames registered via TPEF reference (d). Scale bar: 100 μm. 43

Figure 4. 9. In *vivo* TPEF and OCT *en face* images of the nerve fiber layer (NFL) of a transgenic YFP-labelled mouse taken at 1.3 mW incident laser power and

0.4 NA. Shown are 100 averaged maximum intensity projections (MIPs) from the OCT volumes (left), 100 averaged co-acquired TPEF frames (middle), and their overlayed image (right). Both datasets were registered using the OCT MIPs as reference. 43

Figure 4. 10. In *vivo* Two Photon Excited Fluorescence (TPEF) and OCT *en face* images of the nerve fiber layer (NFL) of a transgenic YFP-labelled mouse taken at 0.625 mW incident laser power and 0.4 NA, with low PMT gain. Shown is a single frame of TPEF and a maximum intensity projection of the same layer from the corresponding OCT volume (a), and then the average of 100 unregistered frames (b), frames registered via OCT reference (c), and frames registered via TPEF reference (d). Scale bar: 100 μm. 44

Figure 4. 11. Averaged TPEF images from the RPE of a mouse before (left) and after (right) TPEF guided motion correction, comprising of 900 frames. 1.2 mW of laser power was used at 0.4 NA. 45

Figure 4. 12. Averages of 100 TPEF images from the RPE layer of a mouse before motion correction (a), after OCT guided motion correction (b), and after TPEF guided motion correction (c). 2.7 mW of laser power was used at 0.4 NA. 46

List of Acronyms

AMD	Age-Related Macular Degeneration
ANSI	American National Standards Institute
AO	Adaptive Optics
APD	Avalanch Photodiode
BS	Beam Splitter
CMOS	Complementary Metal-Oxide-Semiconductor
CNIB	Canadian Nation Institute for the Blind
DC	Dichroic Mirror
DM	Deformable Mirror
FOV	Field of View
FWHM	Full Width at Half Maximum
GFP	Green Fluorescent Protein
GM	Galvanometer Mirror(s)
IPL	Inner Plexiform Layer
MEMS	Micro-Electro-Mechanical Systems
MIP	Maximum Intensity Projection
MIRT	Medical Image Registration Toolbox
MPE	Maximum Permissible Exposure
NA	Numerical Aperture
NADH	Nicotinamide Adenine Dinucleotide
NFL	Nerve Fiber Layer
NIR	Near Infrared
OCT	Optical Coherence Tomography
ONH	Optic Nerve Head
OPL	Outer Plexiform Layer
PBS	Polarization Beam Splitter
PH	Pinhole
PMT	Photomulitpler Tube
PSF	Point Spread Function
QWP	Quarter Wave Plate
RGC	Retinal Ganglion Cell
RPE	Retina Pigment Epithelium

SAO	Sensorless Adaptive Optics
SD	Spectral Domain
SH	Shack-Hartmann
SLO	Scanning Laser/Light Ophthalmoscopy
SNR	Signal-to-Noise Ratio
SS	Swept Source
SVD	Singular-Value Decomposition
TPEF	Two Photon Excited Fluorescence
VFL	Variable Focus Lens
WFS	Wavefront Sensor
WSAO	Wavefront Sensorless Adaptive Optics

Chapter 1.

Introduction

1.1. Overview

Loss of vision is widely viewed to be one of the most disruptive ailments to endure, and currently, ~5.6 million Canadians have eye disease with the potential for permanent vision loss [1]. Because most people will eventually require ocular diagnostics or intervention, the progression of ophthalmological innovation is in society's best interest.

Currently, there many different forms of retinal imaging that can be used to investigate retinal function. This visualization spans various structures within the eye, as well as many fields of view. For larger scale structural information, fundus photography and scanning laser ophthalmoscopy (SLO) are used to visualize the optic nerve head and larger blood vessels. These methods can also incorporate fluorescence to introduce contrast between targets of interest. This can be done intrinsically via autofluorescence, and also extrinsically through the use of injectable contrast agents. One increasingly popular ophthalmic imaging solution is Optical Coherence Tomography (OCT), which is able to provide cross-sectional information about the retina, as well as visualize blood-flow through the use of OCT-Angiography (OCT-A). While these methods can provide microscopic images, their spatial resolution is limited due to the eye being an imperfect objective lens. This can be remedied through the use of adaptive optics (AO) which can counteract these adverse effects. With the improved resolution afforded by AO, cellular resolution imaging becomes possible, which opens the door for imaging of cellular processes, and thus development of techniques for earlier disease detection [2].

The use of animal models in place of humans is widely used in this process of development, and the mouse is the most common specimen. Mice are arguably amongst the most convenient animal models due to their wide availability, ease of care, and especially the presence of extensive genetically engineered strains for the use of disease modelling and labelling of desired features. In order to model the human eye as closely as possible to a clinical setting, *in vivo* imaging is desirable. Being able to non-invasively visualize cellular processes in the retina would allow for many improvements

in disease detection and therapy. This, of course, comes with challenges involving decreased spatial resolution, sample motion, and sample health concerns such as heat damage resulting from the imaging light source.

This thesis will be focused on the employment of improvements to an *in vivo* imaging system for the mouse retina. The aim is to use the mouse model to further develop the system in order to provide solutions currently gating the system's use in humans. In particular, the focus will be on developing functional imaging through molecular contrast.

1.2. The mouse eye

The eye acts as the window for imaging the retina, and as such, it is important to understand it's complexities in order to obtain high fidelity images. It functions much like a modern camera, with a lens controlling the focus of the image, the pupil acting as an aperture to moderate the amount of light coming in, and the retina acting as the sensor to construct the incoming light into an image for the brain (Figure 1.1). While these features exist in both the mouse and human eye, their specifics differ. The human eye is much larger with a focal length of ~22.3 mm and maximum pupil size of ~9 mm, while the mouse eye has a focal length of ~2.6 mm and maximum pupil size of ~2 mm. This means the mouse eye has significantly higher numerical aperture which will prove important for this research. Contrary to the size discrepancy of the eye, their retinas share similar size and function with the mouse retina being ~230 μm and that of humans being ~250 μm. The thickness of the mouse retina relative to the small size of the overall eye leads to a situation referred to as the 'small eye effect', in which considerable amounts of defocus are required to shift a focal plane through the entire thickness of the retina.[3].

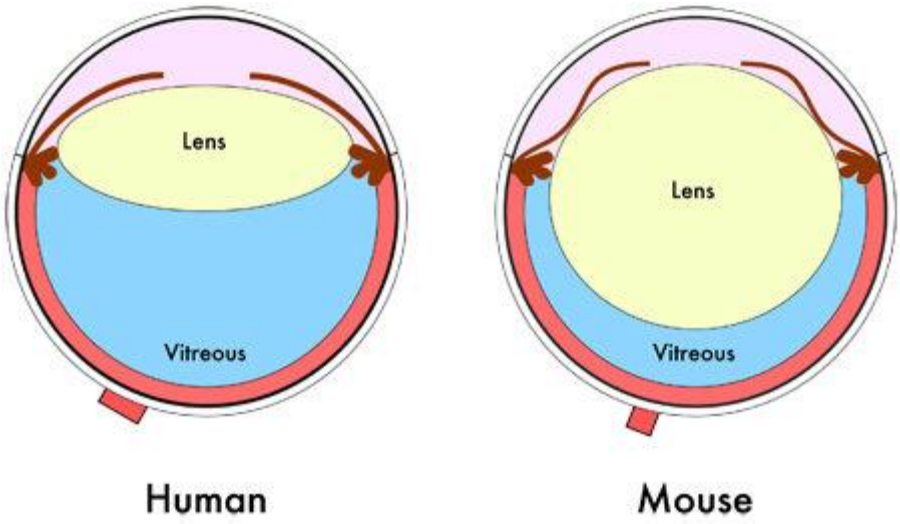

Figure 1. 1. Schematic comparing mouse eye to human eye [4].

The retina itself is a complex structure consisting of several layers of different cell types, each with specific functions (Figure 1.2). Beginning with the most anterior layer, the inner limiting membrane (ILM) is the structural boundary between the retina and the vitreous humor. Next, the nerve fibre layer (NFL) contains the axons connecting to the retinal ganglion cells (RGCs) of the following layer. These structures carry neural signals through the optic nerve head (ONH) to the brain. Moving deeper into the retina is the inner plexiform layer (IPL) which consists of dense fibrils formed by intertwined dendrites of the RGCs. These dendrites are connected to the amacrine and horizontal cells in the inner nuclear layer (INL). These cells process information from photoreceptors and are involved in more complex ocular responses like responding to bright or dim conditions, and recognizing movement of light. The outer plexiform layer (OPL) contains the synaptic terminals between the rods and cones in the following outer nuclear layer (ONL). The rods are highly light-sensitive cells which provide monochromatic light information, and the cones are less light-sensitive, but are better at responding to certain colors. Last is the retinal pigment epithelium (RPE) which supports the light sensing cells and plays a role in vitamin A metabolism [5].

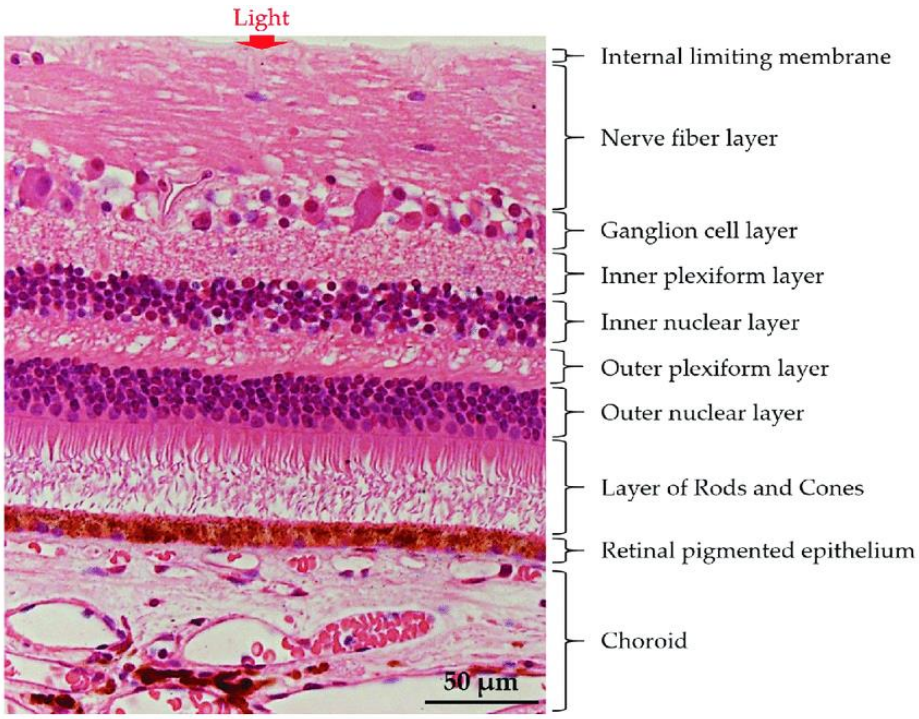

Figure 1. 2. Histological image of retinal layers [6].

In order for an image to be visualized, the retina must first convert light into electrical signals which the brain can process. This process is known as phototransduction and occurs in the rod outer segments and the RPE layer. It begins with the absorption of a photon by a visual pigment molecule in the outer rod segment. This triggers a complex series of chemical reactions, which ultimately produces an electrical signal that can travel through the retina's neuronal network to the brain. After this process occurs, the visual pigment molecule must be recharged before it is able to absorb another photon. This visual cycle alongside the locations of each process is shown in Figure 1.3. Of particular interest to this research, this process generates fluorescent compounds such as retinoids, FAD, and NADH which provides a detectable indicator into the functional health of the retina.

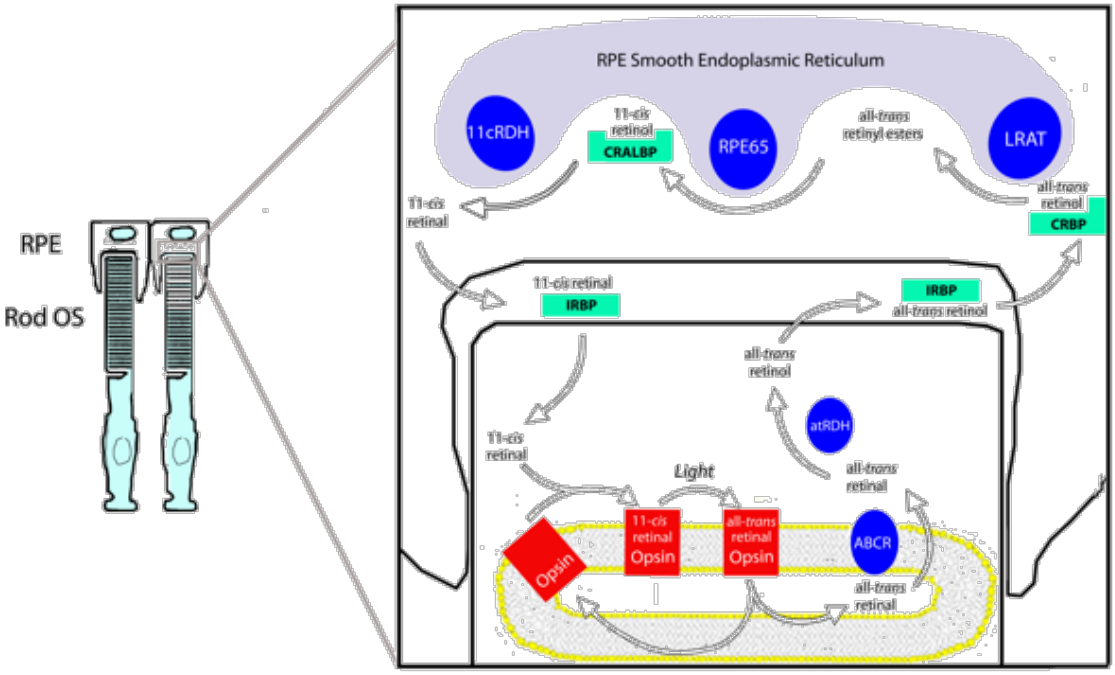

Figure 1. 3. Diagram of the visual cycle between outer rod segments and the RPE [7].

1.3. Imaging the mouse retina

Unlike with most other methods of imaging internal tissues, the eye is conveniently equipped with its own objective lens focused onto the retina. While this allows for many opportunities for non-invasive imaging, it also means that the refractive properties of eye must be considered. The mouse eye in particular possesses both advantages and deleterious properties which alter its ideal imaging conditions.

While the mouse eye can also be imaged via full-field methods such as fundus photography, for this work, we will focus on laser-scanning methods. This method focuses light down to a small spot on the sample, and records the back-scattered or backward directed emitted light to a single pixel. The system then scans across an area to create an image from a defined number of pixels. For this method, the lateral resolution is defined by how small of a spot can be focused onto the sample. For an ideal lens, this spot size is derived from the numerical aperture (NA) of the objective lens. The NA is defined as

$$NA = n \sin \theta, \tag{1.1}$$

where n is the index of refraction and θ is the angle from the optical axis. This results in potentially sub-micrometer resolution, and thus visualization of individual cells. As mentioned, this relationship between spot size and NA is only accurate for an ideal lens and incoming beam. Of course, the objective lens will introduce monochromatic aberrations, especially spherical aberrations in the case of high NA. This effect is especially apparent when using the mouse eye as the objective lens due to its imperfect nature and the presence of biological tissues along the optical path to the retina. These effects compound to increase the spot size, and thus lower the empirical imaging resolution.

In order to achieve diffraction limited results, these effects must be corrected for externally. In recent years, it has become increasingly common to use Adaptive Optics (AO) for this purpose. This method employs deformable optical elements to adjust the incoming wavefront to take shape of the inverse of that which is created by the distortions in the eye (Figure 1.4). Because each eye will introduce different distortions, high-orders of aberrations must be corrected for it to achieve ideal

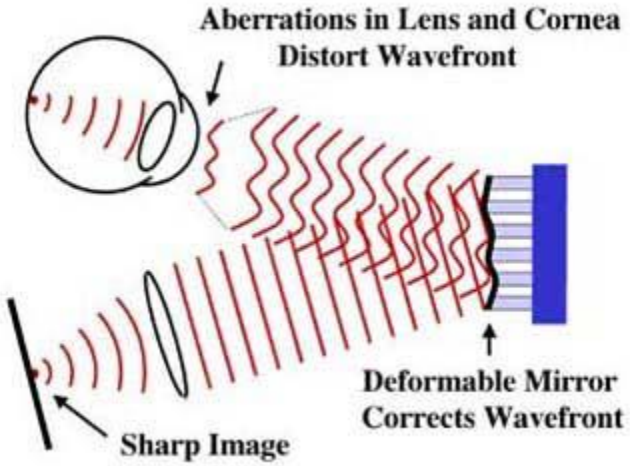

Figure 1. 4. Diagram demonstrating the function of Adaptive Optics [8].

imaging conditions. As such, this technique is preferable over a shaped contact lens which would only correct for a portion of the wavefront error.

In order to correct for these errors, one must have a technique for determining what aberrations are present. The most common method of this is to use a Shack-Hartman Wavefront Sensor (SH-WFS), which consists of a lenslet array preceding a

sensor by one focal length (Figure 1.5). This delivers a physical representation of the shape of the wavefront, which can then be inversely applied to a deformable element.

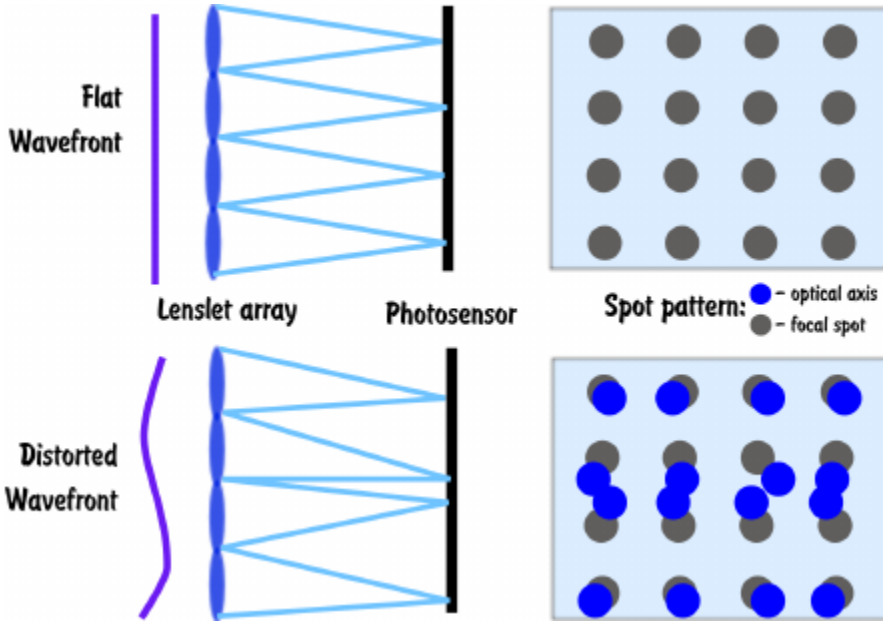

Figure 1. 5. Diagram demonstrating the function of a Shack-Hartmann Wavefront Sensor [9].

Unfortunately, this method is challenging in the mouse eye due to the retina being optically thick relative to the rest of the eye. This causes multiple spots per lenslet which is difficult for wavefront sensing algorithms [3]. Though various groups have shown impressive results from sensor-based AO retinal imaging systems, the work in this thesis will utilize sensorless AO (SAO) [10,11]. This method forgoes the need for a wavefront sensor and generally uses image-based merit functions to determine the aberrations present. Though the current implementations are relatively slow, it avoids the aforementioned complications of using a SH-WFS in the mouse eye, and allows for a more compact imaging system.

1.4. Outline

The remaining chapters of this thesis will provide a background of retinal imaging systems and adaptive optics, and then move to present results from our optical coherence tomography (OCT) and two-photon excited fluorescence (TPEF) scanning laser ophthalmoscope (SLO) experiments. Chapter 2 presents background information on common modalities used in retinal imaging, and the motivations behind our choice of

OCT and TPEF SLO. In addition, adaptive optics and the benefits of multi-modal imaging is discussed. Chapter 3 will present on the optical design of the system, as well as parameter adjustments motivated by software simulations. Following this is preliminary in vivo TPEF SLO images of YFP-labelled retinal ganglion cells (RGCs), demonstrating improved performance from the improved optical design. Chapter 4 demonstrates the aid of OCT in acquiring these TPEF images, through the use of co-registration techniques.

1.5. Contributions

The goal of this work was to continue development on the OCT and TPEF scanning laser ophthalmoscope initially developed by Dr. Daniel Wahl *et al,* with a focus on lowering incident laser power [12]. This came mostly in the form of raising the numerical aperture (NA) of the system, and employing a registration technique which capitalizes on the multi-modal nature of the system.

The first project involved adjustment of the optical design in both the light delivery of the final lens relay, and the capturing of fluorescent light from the sample. After implementing these changes to raise the NA, we experienced difficulties capturing images, so I modelled the system with ray-tracing software to further investigate these changes to the optical design. This informed additional adjustments to the system which are described in Chapter 3, and the results of the simulation were presented at 2020 IEEE Photonics Conference [13]. Once implemented into the system, I was able to acquire TPEF images at considerably lower power than previously possible, within the expected limits permissible for human exposure. These results are shown in Chapter 3, and were presented at 2021 European Conference of Biomedical Optics [14].

When moving to the less efficient endogenous fluorophores in the retina, we had difficulties correcting for motion from the *in vivo* samples. Because of the low laser powers used, individual TPEF frames lacked sufficient features for adequate registration. Because the OCT is acquired simultaneously to the TPEF, I developed an image processing pipeline wherein the OCT is registered, and then these corrections would be applied to the corresponding TPEF frames. Because OCT is a single- rather than a two-photon process, it has superior SNR at low powers, which results in improved motion correction. Preliminary results of this work were presented at 2021 IEEE Photonics

Conference, and final results were presented at 2022 Photonics West Conference, where I demonstrated the effectiveness of the technique on YFP labelled mice. This work is described in Chapter 4 [15,16]. I also utilized this method to image the RPE mosaic of the mouse retina with low laser power, which is presented at the end of Chapter 4.

Chapter 2.

Background on retinal imaging systems and adaptive optics

2.1. Scanning Laser Ophthalmoscopy

Scanning laser ophthalmoscopy (SLO) is a medical imaging technique which provides an *en face* view of the living retina. The technique is based on scanning laser microscopy (SLM) wherein a focal spot is scanned across the sample to build an array of pixels based on the back-scattered or backward emitted light from each position. When using this technique to image the retina, the conventional objective lens is replaced by the eye of the subject, which naturally focuses onto the retina.

There are varying ways to employ this type of imaging apparatus, but they all require a method of scanning the beam, a detector for single pixel detection, and a method of rejecting out-of-plane light. Scanning devices include galvanometer mirrors for variable scan geometries and rates, resonant scanners for high-framerate applications, and MEMS-based scanners for compact solutions. As for detection, it is common to use photo-multiplier tubes (PMTs) and avalanche photodiodes for their high sensitivity. For conventional SLO and SLM, a pinhole is optically conjugated to the focal plane to reject out of focus light. As will be further described in Section 2.3, a method to forgo this confocal pinhole is to use second order imaging techniques like two-photon excited fluorescence (TPEF) which innately restrict signal detection to the focal plane.

Because SLO is a point illumination imaging system, in order to define its resolution characteristics, one must understand diffraction limitations of a focused spot. For a uniform wavefront entering an ideal lens, the light will focus to a point, but due to diffraction effects, this point will take the form of an Airy pattern. The size of this pattern is related to the wavelength (λ) of the light and the NA, which can be thought of as the ratio of diameter to focal length of the lens. Here, the lateral resolution is defined as half the separation distance between the first dark fringe of the diffraction pattern:

$$r_{Airy} = \frac{0.61\,\lambda}{NA}. \tag{2.1}$$

As for the axial resolution, the minimum axial distance for two equally bright objects to be resolved is given by

$$z_{min} = \frac{2\,n\,\lambda}{NA^2}, \tag{2.2}$$

where n is the diffractive index of the medium [17,18]. While this definition of lateral resolution will be accurate, the definition of axial resolution will be adjusted due to TPEF's rejection of out-of-focus light. This will be discussed further in section 2.3**.**

Of course, these theoretical limits are defined for an ideal lens, which we have discussed to not be the case for this project. Thus, in order to restore the system's resolution to the theoretical limit, aberrations will require correction via AO, which will be discussed in Section 2.4.

2.2. Optical Coherence Tomography

Optical Coherence Tomography (OCT) is an imaging method that uses coherence gating techniques in order to obtain high-resolution volumetric data from back-reflection within the sample. While the method can be conducted via full-field methods, we will focus on scanning-laser methods which is more applicable to our SLO system. Similarly to SLO, a focal spot from a light source is scanned across the sample to create an array of pixels, but in this case, each pixel is an intensity depth profile (A-scan). From this array of depth profiles, one can visualize both cross-sections (B-scans) of the sample, and *en face* views from any depth.

There are two main methods of acquiring OCT data: Time Domain and Fourier Domain (FD) OCT. Both methods are based on a Michelson interferometer and a low-coherence light source, with the former selecting axial depth by translating the reference arm. While this method has some modern applications, it has much slower operating speed than FD-OCT and thus the latter is much more frequently used. FD-OCT itself can be further split into the two categories of Swept Source (SS) OCT and Spectral Domain (SD) OCT, with the former using a single detector and a laser that sweeps through the spectral range, and the latter using an array of detectors to measure the interference pattern via spectrometer.

To conduct OCT, the light source is split into a sample and a reference arm. The reference light is reflected off a path matched mirror, and the sample light is reflected off the sample, before both paths are recombined at a fibre coupler. The interference pattern is then measured, where higher frequency fringes correspond to a larger path length difference between the two paths. Thus, by calculating the Fourier transform, one can determine the axial location of this back-scattered light.

The axial resolution of a FD-OCT system is defined by the coherence length of the light source, given by equation 2.3:

$$l_c = \frac{2\ln 2}{\pi} \cdot \frac{\lambda_o^2}{\Delta\lambda}, \tag{2.3}$$

where λ_0 is the center wavelength, and $\Delta\lambda$ is the spectral bandwidth of the light source. For a scanning laser configuration like in this thesis, the lateral resolution is determined by the size of the focal spot, as described in Section 2.1.

2.3. Fluorescence Imaging

Fluorescence imaging is a technique commonly used in biological imaging which can provide contrast between optically similar subjects. This can be done both intrinsically and extrinsically with both having unique advantages and difficulties. Green Fluorescent Protein (GFP) is commonly used to label relevant cells in animal studies, which allows one to distinguish these cells between others with similar optical properties, or to image transparent cells which would otherwise not be detectable via back-reflection techniques. As well as genetic labels, fluorescent dyes such as fluorescein can be injected or ingested to target various functional processes as the compounds are metabolized. As for intrinsic fluorophores, it is common for biological samples to have autofluorescent properties which can often provide insight into the health of the tissue [19–21]. The trade-off between these two methods of fluorescent imaging is that introduced fluorophores are often bright, but need to be injected or ingested which can be uncomfortable and time consuming; whilst intrinsic fluorophores are often very dim and need very sensitive detection, but provide unique insights to the function of the sample in a completely non-invasive, time-sensitive manner.

Acquiring a fluorescence image is relatively simple, with the key factor being the phenomenon known as the Stokes Shift. When a fluorophore absorbs a photon's energy

and is excited above the ground state, after some time, the molecule relaxes back down to the ground state and emits this loss of energy in the form of light. In most cases, this emitted light has lower energy, and thus a longer wavelength than the absorbed light. This change in wavelength is the Stokes Shift, and through the use of chromatic filters, one can separate the back-reflected light from this fluorescent light.

One drawback of this technique for our scanning-laser applications is that fluorescence would be present throughout the entire optical path in the sample, rather than restricted only to the focal plane. As well as this, the fluorophores intrinsic to biological tissue are commonly excited in the near-UV range, which severely limits imaging depth due to tissue's high optical attenuation at these wavelengths. One method to address these concerns is to use two-photon excited fluorescence (TPEF). This process can occur when two photons of half energy excite the fluorophore in a single quantum event. The time-scale for this to occur is extremely short, so to achieve a sufficient number of these events to acquire images, a very high photon flux is required. Because of these two features, TPEF often uses near infrared (NIR) light which is less attenuated than UV light, and the excitation is limited to the focal spot which improves resolution and forgoes the need for a confocal pinhole.

In order to achieve the high photon flux required for two-photon events, TPEF imaging systems utilize ultrashort pulses of light to improve SNR without the need for extraordinarily high average power which would ultimately damage the sample. Additional parameters for increasing TPEF signal can be deduced from equation 2.4,

$$n \approx \frac{P^2 \sigma}{\tau_p f_p^2} \left(\frac{NA^2}{hc\,\lambda} \right)^2, \tag{2.4}$$

Where n is the number of photons absorbed, P is the average incident power, σ is the cross-section of the fluorophore, τ_p is the laser pulse width, f_p is the pulse repetition rate, NA is the numerical aperture, and λ is the wavelength of the source light [22]. From here, we see that the probability of a two-photon event scales with the NA to the fourth power, which makes this parameter paramount for TPEF imaging systems.

2.4. Adaptive Optics for Ophthalmic Imaging

Adaptive Optics is a technique used in a wide variety of optical systems where turbid media distorts the image. It was originally developed as a technique for astronomy to correct image distortions caused by atmospheric turbulence. From here, the technology began moving to other applications where the optical path contains media detrimental to the incoming and outgoing wavefront. One application was for *in vivo* biological imaging where it is common that the sample contains unpredictable imperfections. More specifically, AO suits retinal imaging well due humans' common imperfections of their cornea and lens [23]. Regardless of the application, AO requires an active optical element to correct for the measured distortions, as well as a method to detect them.

The correction can be applied by a variety of deformable elements, such as a multi-actuator adaptive lens (MAAL) or a deformable mirror (DM) [24,25]. Of course, each technique has advantages and drawbacks, with the MAAL allowing for compact design, but lacking corrective power, and the DM boasting superior corrective power whilst being relatively bulky. For the purposes of this thesis, we focused on the use of DM's which better satisfy our needs.

For wavefront measurement, it is typical to use a Shack-Hartmann (SH) wavefront sensor (WFS) [26–28]. This device consists of a lenslet array which precedes a detector by one focal length. The lenslet array is a grid of small identical lenses, which will form an array of spots on the detector. If the incoming wavefront is perfectly flat, it will produce an evenly spaced grid of spots, but if the wavefront has any distortions, these spots will experience a corresponding displacement on the sensor (Figure 1.5). Through the use of software, a gradient map can then be created using the displacement of the spots.

The quality of the focal spot is related to this wavefront in that the PSF is given by this wavefront's 2D Fourier transform [29]. From this, we can see that any frequency content introduced to the wavefront via aberrations will result in a larger focal spot after the objective lens. These wavefront aberrations, $W(\rho,\theta)$, are commonly represented in the form

$$W(\rho,\theta) = \sum_{j=0} a_j Z_j(\rho,\theta), \tag{2.3}$$

where Z_j is the j^{th} order of the orthogonal polynomial set known as the Zernike polynomials, and a_j is the corresponding coefficient of that order [30]. The first 14 orders are listed in Table 2.1 alongside their classical name and mathematical representation.

Table 2.1. Zernike polynomials and names up to 14th index [31]**.**

Index (j)	*Classical Name*	*Zernike Polynomial* $\boldsymbol{Z_j(\rho,\theta)}$
0	Piston	1
1	Tilt	$2\rho\sin\theta$
2	Tip	$2\rho\cos\theta$
3	Oblique astigmatism	$\sqrt{6}\rho^2\sin 2\theta$
4	Defocus	$\sqrt{3}(2\rho^2-1)$
5	Vertical astigmatism	$\sqrt{6}\rho^2\cos 2\theta$
6	Vertical trefoil	$\sqrt{8}\rho^3\sin 3\theta$
7	Vertical coma	$\sqrt{8}(3\rho^3-2\rho)\sin\theta$
8	Horizontal coma	$\sqrt{8}(3\rho^3-2\rho)\cos\theta$
9	Oblique trefoil	$\sqrt{8}\rho^3\cos 3\theta$
10	Oblique quadrafoil	$\sqrt{10}\rho^4\sin 4\theta$
11	Oblique secondary astigmatism	$\sqrt{10}(4\rho^4-3\rho^2)\sin 2\theta$
12	Primary spherical	$\sqrt{5}(6\rho^4-6\rho^2+1)$
13	Vertical secondary astigmatism	$\sqrt{10}(4\rho^4-3\rho^2)\cos 2\theta$
14	Vertical quadrafoil	$\sqrt{10}\rho^4\cos 4\theta$

These polynomials are convenient for representing optical aberrations for many reasons. For one, their representation over the continuous unit circle well represents optical wavefronts which are typically circular. As well as this, they well describe common optical aberrations such as spherical aberration, coma, and astigmatism. Finally, because they form a complete orthogonal basis set, one has much freedom in how accurately they wish to represent the wavefront, because additional orders can always be added.

Compiling these concepts and devices into a typical AO system for retinal imaging, one must utilize what is commonly referred to as a guide star. The term originates from astronomy where an artificial star is created by shining a bright laser into the sky. Depending on the illumination method, this laser light is either reflected, or

causes fluorescence in the atmosphere, which provides the telescope with a signal representative of the distortions that a perfect point source would experience. The same concept applies in retinal imaging, but instead of the atmosphere, it's the retina. As such, the back-reflected point source (called a beacon) forms the wavefront at the pupil plane for the SH-WFS to measure. The deformable element, in our case a DM, will then take shape of the complex conjugate of the measure wavefront to correct the distorted wavefront. This process can be conducted in an open- or closed-loop configuration such that the process can be repeated until the desired image quality is achieved [32].

Unfortunately, as shown in Section 1.3, this approach is challenging in the mouse eye due to scattering from multiple retinal layers. This results in the guide star producing multiple spots per lenslet or the lenslet spots being bi-modal which complicates the centroiding process [3].

For our experiments, we chose to use a sensorless approach to aberration correction. This method works by applying aberrations to the DM, and taking note of its effect on the image. Consider applying a single Zernike order to the DM over a range of coefficient values whilst recording the image quality at each value. One of these values will provide the best image quality, and thus the amount of that Zernike order present in the wavefront has been inversely deduced [33]. This can then be repeated for as many Zernike orders as one needs depending on their tolerance for error, and the capabilities of the deformable element. This is, of course, a simplification of the optimization problem, and will be further discussed in Chapter 3.

2.5. Multimodal Imaging for Non-Invasive Applications

When performing any *in vivo* imaging, it is, of course, of utmost importance to avoid damaging the sample. This becomes exceptionally important in the case of retinal imaging due to the light sensitive nature of the tissue. As such, the laser power incident on the eye must be very low, much lower than most other *in vivo* imaging applications. As mentioned in Chapter 1, OCT is an increasingly popular ophthalmic imaging technique. It allows for volumetric imaging at very low incident powers which do not damage the eye. However, while it provides volumetric data at impressive resolution, it lacks the functional imaging capabilities of some other modalities. As mentioned in Chapter 2.3, one functional imaging technique of note is that of fluorescence imaging.

With the aid of AO, it can provide these functional images at diffraction limited resolution, though due to the limitations on imaging power, it provides a relatively dim signal, and it can be difficult to acquire images of the desired features. This difficulty is two-fold: due to the small amount of signal, images require long exposure times which blur the images, and without live feedback of the system's field of view (FOV), aligning the sample becomes challenging. Thus, in order to maintain these low incident powers without sacrificing image fidelity, it becomes enticing to use these two modalities in a complementary fashion [34].

By performing both of these imaging techniques simultaneously with the same light source, we can benefit from both without a significant increase in system complexity, as well as use one to compliment the other [35]. In this thesis, we will see that the majority of sample alignment and initial AO correction was conducted using an OCT signal. This is due to the fluorescence signal being so initially weak that it is unable to provide any live feedback without raising laser powers to potentially damaging levels. As well as this, because of the aforementioned need for long exposure times, we designed the system such that we could utilize the OCT signal to perform non-rigid registration, and apply these image transformations to the fluorescence signal. This is because the fluorescence signal is often too dim for registration techniques to be effective due to lack of features in each image. This will be further discussed in Chapter 3 where it will become clear how imperative this multi-modal technique is to our imaging work-flow.

2.6. Summary

This chapter provided an outline on retinal imaging systems and adaptive optics, with a focus on OCT and fluorescence-based imaging techniques. Multi-modality was also discussed in brief, as well as its importance in maintaining non-invasiveness for fluorescence imaging in the retina. The remaining chapters will build upon these topics in increasing complexity, demonstrating our experimental results with the imaging system.

Chapter 3.

Wavefront sensorless adaptive optics TPEF for *in vivo* retinal imaging in mice

3.1. Introduction

Retinal imaging is a valuable clinical tool for ophthalmology and can be used to detect a range of diseases. Early detection and thus intervention can result in prevention of permanent vision loss. Fluorescence imaging is a versatile modality in visual science due to a diverse set of extrinsic and intrinsic fluorophores available for retinal imaging. For example, relevant cells can be labelled with Yellow Fluorescent Protein (YFP), and autofluorescence can be detected from the Retinal Pigment Epithelium (RPE), with the latter being of note due to its relation to diseases such as Age Related Macular Degeneration and Stargardt disease [2,36,37]**.** Optical Coherence Tomography (OCT) provides structural imaging capabilities, which is highly complementary to the molecular contrast generated from fluorescence. Together, these two methods could be used to greatly further the development of therapies for vision robbing diseases [38–41].

Detection of the fluorophores in the retina is difficult due to a variety of factors, including: low power levels, scattering in the retina, and attenuation of near-UV wavelengths in the vitreous humor. To circumvent these issues, Two-Photon Excited Fluorescence (TPEF) is a viable option due to the use of longer wavelengths and inherent axial sectioning. In order to avoid damaging the light sensitive tissue of the retina with TPEF, the average power must be kept low, and thus we use a pulsed laser to achieve the required photon density. Also, a high numerical aperture (NA) configuration is desirable for maintaining low laser power due to TPEF's efficiency scaling with NA to the fourth power [42]. With the eye acting as the objective lens of the system, raising the NA is restricted to increases in beam diameter, and unfortunately introduces monochromatic aberrations that severely distort the focal spot, which results in significantly dimmed TPEF images.

To avoid the adverse effects of these aberrations, we use adaptive optics (AO) to minimize the focal spot on the retina. Often, a wavefront sensor is used to detect aberrations, but this technique proves difficult for mouse retinal imaging. Due to the

mouse retina's relative thickness compared to the rest of the eye, reflections from multiple layers cause single lenslets to produce multiple spots, which confuses the centroiding process [3]. To combat this, we forgo the wavefront sensor for an image-based sensor-less algorithm. It optimizes via a hill-climbing coordinate search of 21 Zernike modes and uses the sharpness of the en face image as a metric.

The work in this thesis involves continued development and improvement of an OCT and TPEF biomicroscope initially developed by Dr. Daniel Wahl [12]. In this chapter, we present the changes to this imaging system which allowed for near diffraction limited TPEF imaging of the cellular makeup of the mouse retina, when used in conjunction with SAO and OCT. This began with a modeling of the system in Zemax Optic Studio in order to better visualize the system's performance under various alterations. These results de-risked our proposed system improvements, and also demonstrated some necessary improvements to the system which were not originally anticipated. These changes provided the expected empirical results, and allowed for imaging of YFP labelled ganglion cells at reduced incident, power without sacrificing image fidelity.

3.2. Methods

3.2.1. Mouse Handling

For the experiments of this section, we used YFP-labelled mice of the strain B6.Cg-Tg(Thy1-YFP)16Jrs/J obtained from Jackson Laboratories (Bar Harbor, ME) whose ganglion and neuronal cells contain YFP. The imaging conditions were compliant to the Canadian Council on Animal Care, and were performed with the approval of the University Animal Care Committee at Simon Fraser University. Before an imaging session, the chosen mice would be subcutaneously injected with an anesthetic cocktail of ketamine (100 mg/kg of body weight) and dexmedetomidine (0.1 mg/kg of body weight). Once anesthetized, drops of 1% Tropicamide were applied to the eyes to maximally dilate the pupils. Lastly, a 0-diopter rigid contact lens was applied to each eye to prevent corneal dehydration.

3.2.2. Optical Design

A schematic of the inherited SAO OCT TPEF imaging system is shown in Figure 3.1. One light source was used for both the OCT and TPEF, which was a femto-second pulsed laser (Mai Tai HP, Spectra-Physics, CA, USA) and the center wavelength could be tuned from 690 nm to 1040 nm. This results in a spectral bandwidth between 8 and 16 nm, and thus an axial resolution in the OCT between 16 and 22 µm. A variable focus lens (VFL,A-39N1, Corning, USA) was used to change the axial location of the focal spot to image different depths in the retina. Following this is the deformable mirror (DM; DM-69, ALPAO, France) for aberration correction, and an XY mounted pair of galvanometer-scanning mirrors (GM, 6215H, Cambridge Technology Inc., USA) to scan the focal spot across the retina. These three elements were optically conjugated to the mouse eye with lens-based relays constructed with achromatic doublets.

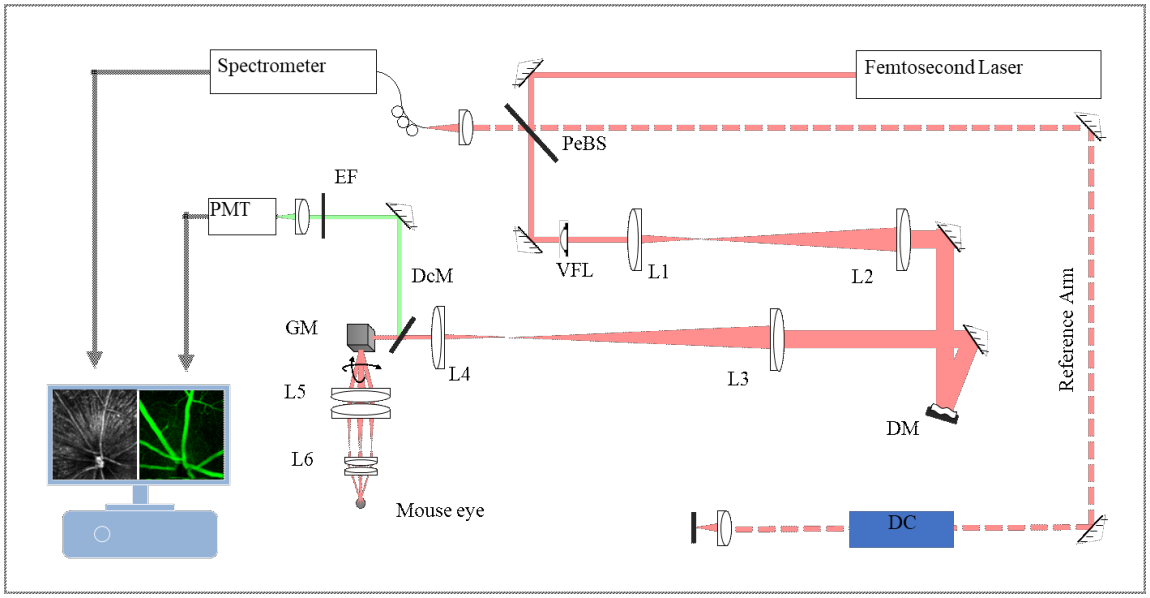

Figure 3. 1. Schematic of the SAO OCT and TPEF imaging system. The imaging system was constructed with a pellicle beam splitter (PeBS), variable focus lens (VFL), deformable mirror (DM), dichroic mirror (DcM), galvanometer-scanning mirrors (GM), emission filters (EF), photo-multiplier tube (PMT), dispersion compensation (DC), and the following lenses: L1=100 mm, L2=300 mm, L3=400 mm, L4=100 mm, L5=2x125 mm, L6=2x50 mm. The reference arm denoted as a dashed line [12].

The back-scattered light from the excitation was recombined with the light from the reference arm and coupled into a single mode fibre before reaching a custom-built spectrometer (Bioptigen Inc., USA) with a spectral range from ~730 to ~995 nm. The

generated inference pattern cane then be processed into volumes using a custom GPU-accelerated program for real-time processing and display [43,44]. The A-scan rate of the OCT was 100 kHz, with a sampling density of 1024 x 400 x 200

In this configuration, the TPEF emission signal was de-scanned by the GM before being reflected by a dichroic mirror (DcM) into the photo-multiplier tube (PMT, H7422P-40, Hamamatsu Photonics, Japan). The digitization of the PMT signal was synchronized with the OCT A-scans to ensure that it and the TPEF could be operated simultaneously and were co-registered. This gives the TPEF images complimentary information on 3D structure, providing retinal landmarks to identify where the image was acquired. The OCT could be deactivated to achieve faster TPEF acquisition, up to 10 frames per second, for cases where there was a sufficiently bright signal.

3.2.3. Adaptive Optics Optimization

The image optimization via adaptive optics were done via a hill climbing Coordinate Search (CS) algorithm where the merit function is derived from either the OCT or TPEF image [45]. This merit function is defined by the image sharpness (S_{img}), which is calculated by summing the squared intensity of each pixel across the image in the form

$$S_{img} = \sum_{x,y} [I(x,y)]^2. \tag{3.1}$$

Here, *I(x,y)* is the intensity of the pixel at location *x, y*. During the optimization algorithm, the image resolution would be decreased from 400x400 pixels to 400x100 pixels in order to allow for significantly faster run times at approximately 30 seconds.

To initialize the algorithm, one must choose which Zernike modes to search through. For this thesis, we would begin with defocus, and then the astigmatisms before searching up until the 21st mode due to diminishing returns past this point. For each mode, the DM would begin flat, and then apply a range of coefficients $\pm a_j$ to the corresponding mode Z_j as in Equation 2.3. The merit function would be evaluated at each coefficient value, and then a then a second-order polynomial would be fit to the values to solve for what coefficient results in maximum image sharpness. This optimum coefficient a_j would then be applied to the DM before moving onto the next mode. This

process would be repeated for each Zernike order until the 21st was reached. In order to achieve the best possible image, this process would be repeated between 3 and 5 times until optimization runs would provide no improvement to the image quality [46]. The range and spacing of the coefficients could be easily chosen between optimization runs depending on the stroke required to correct the image, and how quickly one would want the algorithm to complete.

3.3. Results

3.3.1. Design considerations via Zemax Optic Studio

The design improvements began with the optics for capturing of the fluorescent light. As seen in Figure 3.1, the collimated light from the GM is demagnified by approximately 2.5 mm to 1 mm. When a TPEF event occurs, it can be treated as a point source, which means that the light fills the mouse's pupil on the backwards path. Because the mouse pupil has an aperture of ~2 mm, this means that before the light is de-scanned by the GM, it will be magnified by 2.5 times to approximately 5 mm, which is double the clear aperture of the galvanometer mirrors. Because we were not yet able to account for the increased aberrations of utilizing the full mouse eye aperture, we altered the TPEF detection path by placing the DcM between the final relay lenses. The lens used to focus the fluorescent light into the PMT was an A-coated 60 mm achromat. The lens was placed approximately 110 mm from the final relay lens in order to lightly focus the captured light into the PMT. Due to space constraints, we were not able to shrink the beam with a relay, and because the PMT simply integrates over all light captured per pixel, we did not require an in-focus image. This reduced the fluorescent light lost in the backwards path, whilst allowing us to maintain an incident beam of smaller diameter than the mouse pupil. This change is shown schematically in Figure 3.2. This alteration was successful, and *in vivo* results will follow in Section 3.3.2.

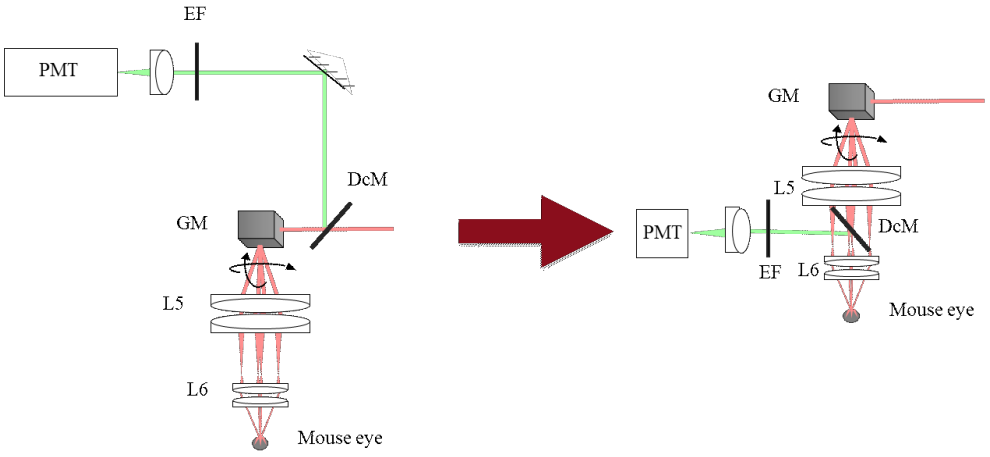

Figure 3. 2. Schematic of the changes made to the TPEF detection path on the SAO OCT and TPEF imaging system. Dichroic mirror (DcM) was moved to between final relay lenses to avoid loss of signal when de-scanned by galvanometer mirrors (GM). Lenses shown are L5=2x125 mm, L6=2x50 mm to optically relay GM to mouse pupil, and PMT focusing lens 60 mm.

Following this, we began to investigate the various implications of raising the numerical aperture (NA). As described in Chapter 2, the TPEF efficiency scales with NA to the fourth power, so in order to maintain low laser powers, raising the NA is a priority. We accomplished this by changing the final relay lenses L5 and L6 from 2x125 mm and 2x50 mm respectively, to 2x100 mm and 30 mm for a change in demagnification from 2.5x to 1.6x. This resulted in a change in beam diameter from 1 to 1.5 mm, and change of NA from 0.25 to 0.4. Unfortunately, after implementing these changes, we had difficulty imaging the nerve fibre layers of our transgenic mice. Because of this, we chose to model the system in the ray tracing software Zemax Optic Studio such that we could diagnose the issue.

A sample of the forward path simulation is shown in Figure 3.3. This model used stock lenses from the Thorlabs lens catalogue, a model of the Variable Focus Lens provided by Corning (VFL, Arctic 39N0, Corning, NY, USA), and a model mouse eye [47]. The VFL model allowed for focus control via adjustment of the simulated input voltage, and well simulated the expected response of the element. The mouse eye allowed for a coarse interpretation of the response from *in vivo* imaging, but due to its

lack of high-order aberrations and imperfections, conclusions from its results were reserved.

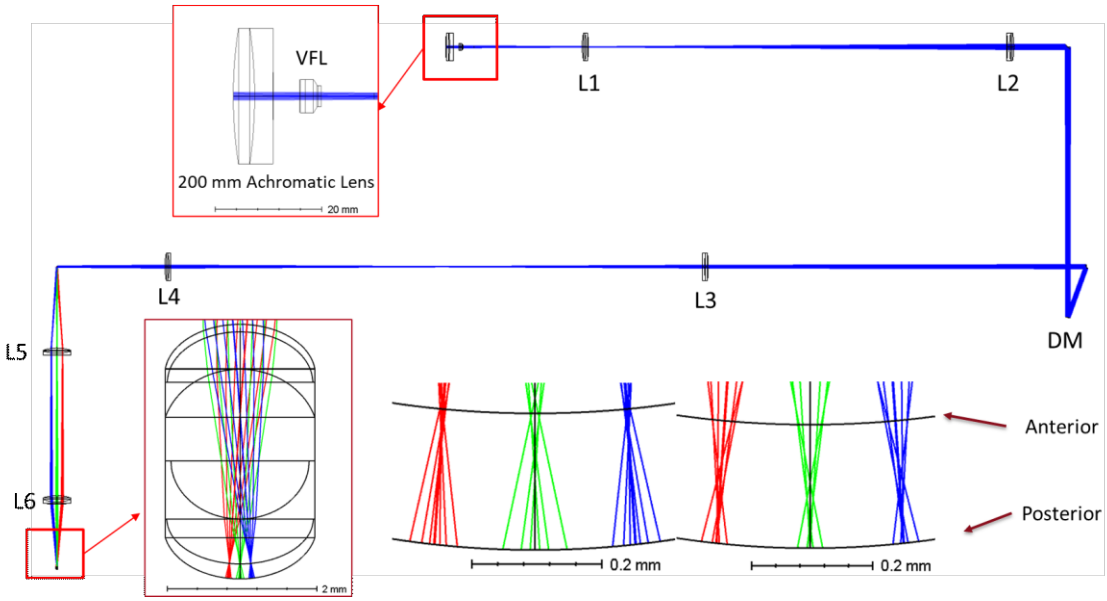

Figure 3. 3. A simulation of the forward path of the SAO OCT and TPEF imaging system using Zemax Optic Studio. A model mouse eye was used, where the anterior and posterior segments of the retina are shown with a $\pm 2^{o}$ scan [Gardner et al mouse eye]. L1=100 mm, L2=300 mm, L3=400 mm, L4=100 mm, L5=2x100 mm, L6=50 mm.

One of the first conclusions made from this simulation was the inability of the system to focus on the anterior segments of the retina. The eye naturally focuses on the posterior segment of the retina where the photoreceptor cells are located. For our experiments pertaining to the YFP-labelled ganglion cells, our aim was to utilize the VFL to increase the focusing power in real-time in order to shift the focus to these anterior layers. This worked well for our experiments at 0.25 NA, but after increasing to 0.4, the VFL was unable to provide enough optical power to maintain this shift in focal length. Because we have no use for extending the focus past the photoreceptor layer, we implemented a 200 mm focal length lens immediately preceding the VFL in order to shift its range from -5 to 15 diopters to 0 to 20 diopters. This allowed for axial sectioning power ranging the entirety of the retina which can be seen in Figure 3.4. As we will see

in section 3.3.2, this allowed for the system to image the ganglion cells and nerve fibre layers at our increased NA.

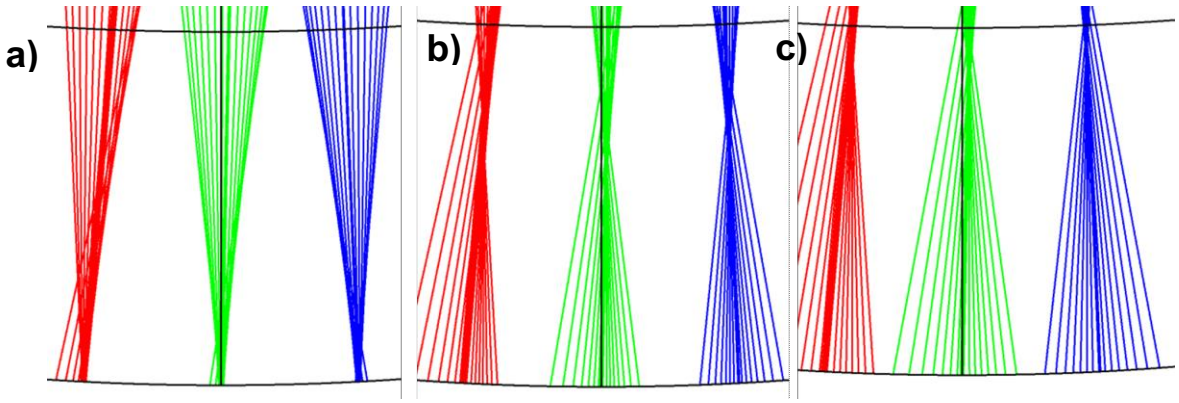

Figure 3. 4. A simulation of the foci generated in the mouse retina under a $\pm 1^{o}$ scan. Shown is a scan with a 0 diopter contribution from the VFL (a), 15 diopters (b), and 20 diopters after preceding the VFL a 200 mm focal length achromatic doublet (c).

Next, it was important to isolate the origin of the aberrations to confirm that the majority are caused by the mouse eye rather than system error. We accomplished this by measuring the aberrations present at the pupil of the mouse eye under varying conditions consistent with imaging conditions. Figure 3.5 shows the initial results of this, where the aberrations introduced by the VFL were investigated. Here, the vergence of the VFL was adjusted, which introduced some expected distortions to the image. The plot shows the recorded Zernike coefficient for orders between 4 and 15 due to the majority being found in this range. The majority comes from spherical aberration which is to be expected due to spherical aberration's connection to NA, which is of course increased when raising the lens' vergence.

We also performed this experiment with a 2-degree scan angle from the galvanometer mirrors. While we use much larger FOVs for locating areas of interest, this is the largest FOV we would expect to use for our *in vivo* experiments with aberration correction. From Figure 3.6, we see that this introduces contributions from horizontal coma, which is the expected aberration when a spherical beam enters a lens horizontally off-axis. The effect of this increases with higher VFL vergence, but as we will see, the overall effect was negligible in comparison to the mouse eye.

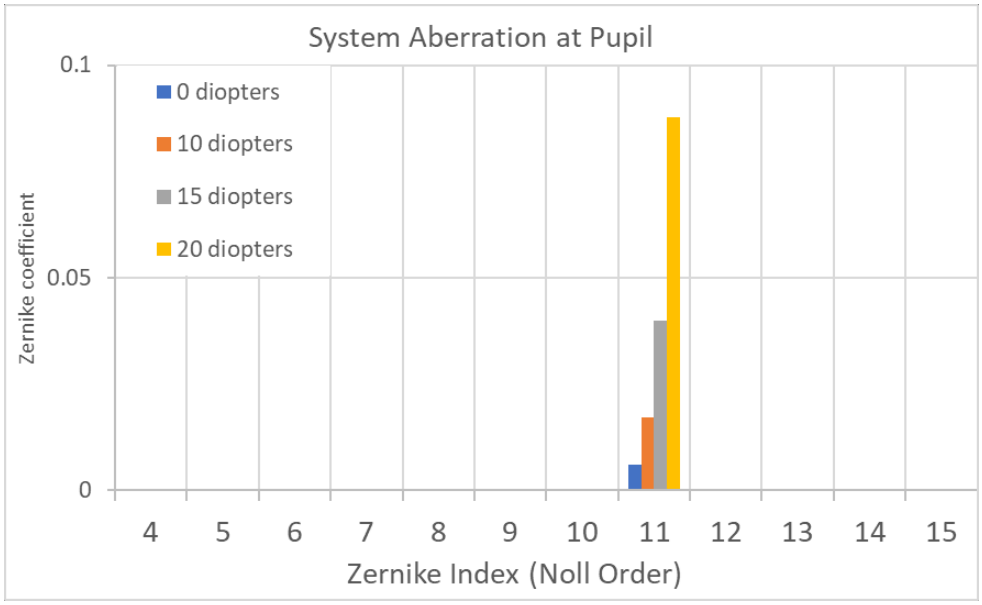

Figure 3. 5. A chart from Zemax simulation displaying system aberrations under varying VFL curvatures ranging from 0 to 20 diopters. Data is displayed as Zernike coefficient versus Zernike index.

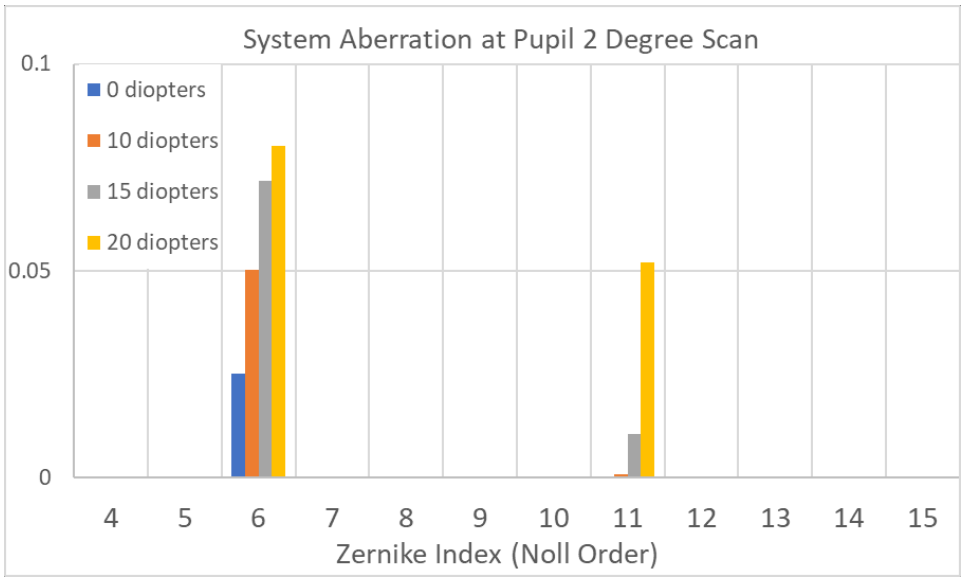

Figure 3. 6. A chart from Zemax simulation displaying system aberrations under varying VFL curvatures ranging from 0 to 20 diopters under influence of $\pm 2^{o}$ scan via galvanometer mirrors. Data is displayed as Zernike coefficient versus Zernike index.

As such, we next investigated via our simulation the comparative magnitude of system aberrations against that of the mouse eye, in order to determine whether the aberrations present from the increased NA were too great to be corrected by the DM. These results are shown in Figure 3.7, where data was taken for an on-axis beam for both a mouse eye square with the optical axis, and with a 3-degree rotation about the vertical axis. This was, again, intended to well represent common imaging conditions such as when features of interest are located outside the macula. Comparing these values to the system aberrations, they are approximately 2 orders of magnitude larger, and therefore dominating the overall distortions as expected. The indices of these Zernike modes are as expected too, with the on-axis beam displaying only spherical aberration, and the off axis introducing some primary horizontal astigmatism, but primarily horizontal coma due to asymmetry about the optical axis. While the system in lieu of a mouse eye displayed near diffraction limited performance, its introduction puts the system about 2 orders higher than the Maréchal criterion. With the aid of the DM, however, because the total RMS error is less than our maximum DM stroke of 80 μm, we can correct for these distortions to maintain near diffraction limited imaging conditions.

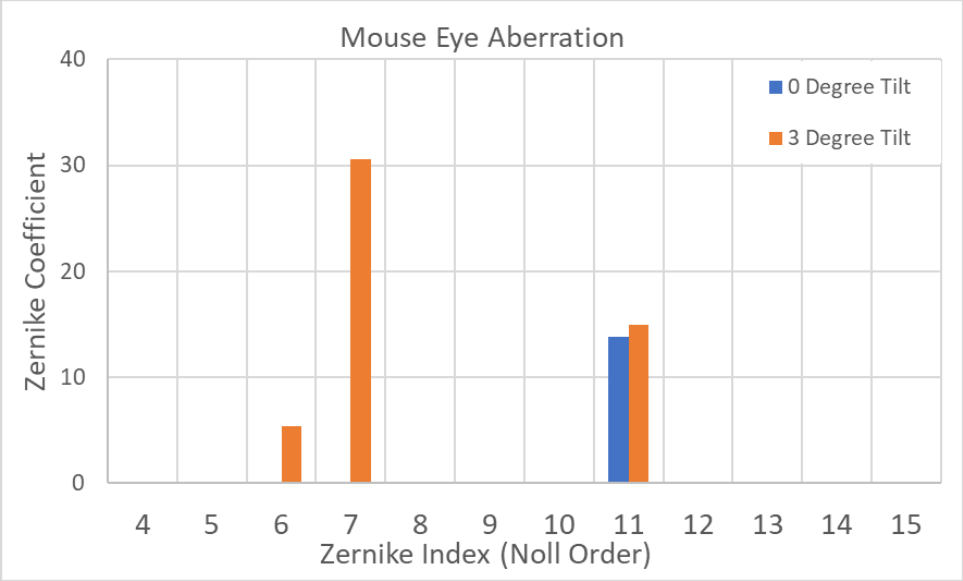

Figure 3. 7. A chart from Zemax simulation displaying aberrations present at the focal plane of a mouse imaging configuration. Results were taken for an on-axis beam for both a mouse eye square with the optical axis, and with a 3-degree rotation about the vertical axis.

3.3.2. *In vivo* WSAO TPEF with increased numerical aperture

With these simulated changes implemented into the imaging system, we were able to visualize the sensory neurons of our transgenic YFP-labelled mice at lower incident power than the previous work**,** without sacrificing image fidelity [12,45].

Because the system in designed for *in vivo* imaging, sample motion must be taken into account due to breathing which causes large translations at our small FOV's (~100 μm). Thus, the integration time for each pixel is kept short so that we are able to average many frames in post-processing, rather than have a single image with uncorrectable motion. Figure 3.8 shows TPEF SLO images from a sample of lens tissue soaked with fluorescein, where the left shows a single frame, and the right an average of 200 frames. From here, we can see that a single frame has poor SNR, and thus many frames must be averaged. For the case of a static phantom, this process is very simple, but for *in vivo* imaging, the motion must be corrected before averaging can be performed.

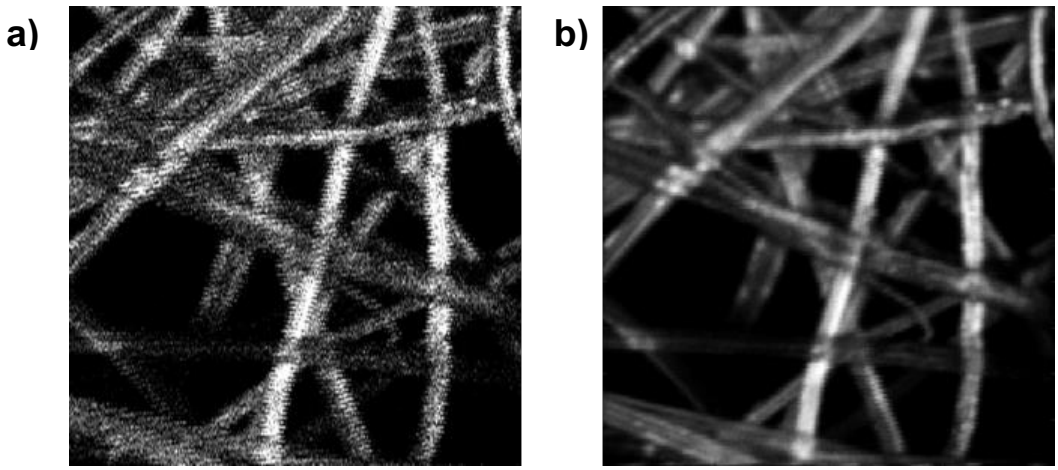

Figure 3. 8. TPEF SLO images from a sample of lens tissue soaked with fluorescein, showing both a single frame (a), and an average of 200 frames (b).

A relatively simple algorithm was used to correct for motion prior to averaging. 1) First, a single frame was manually selected as a registration target; 2) Rigid registration was applied such that each frame was vertically and horizontally translated until cross-

correlation with the target was maximized; 3) Each row of the image was translated horizontally and vertically such to maximize the cross-correlation with the target [48,49]; 4) The frames were non-rigidly registered to the target via sum of squared difference similarity metric along cubic B-splines, which utilized the Medical Image Registration Toolbox (MIRT) [50]; 5) Lastly, the frames were averaged, and the upper and lower thresholds were manually adjusted to provide optimum brightness and contrast.

Figure 3.9 shows *in vivo* TPEF images of the nerve fibre layer of a transgenic YFP-labelled mouse, taken with a center wavelength of 940 nm. The top row shows images at 0.25 NA and 2.5 mW before adjustments to the incident beam size, and the bottom row at 0.40 NA and 1.3 mW after the design changes were implemented. The left column displays images in absence of any SAO corrections, and the right after SAO corrections where the TPEF image sharpness was used as the optimization metric. These images consist of 200 SLO frames acquired in approximately 20 seconds, and were processed using the procedure outlined above.

As expected, in the absence of AO, the image with higher NA in Figure 3.9 has significantly lower SNR due to the increased aberrations. As for the images with AO corrections, because of the 60 percent increase in NA, from theory (Eqn. 2.4), we should expect an approximately 6 times brighter image. Here, however, we lowered the power by half which would dim the image by 4 times, so we should expect an image about 1.5 times as bright. While the features do appear somewhat brighter with increased contrast against the background, the SNR only experienced an increase of 20 percent. This could be due to a variety of factors such as the blurred edges of the features from inadequate registration, clarity of the mouse cornea, or inaccurate mouse alignment. As for the registrations, when each frame is extraordinarily dim, it can be difficult for the registration algorithm to perform as expected. This issue is addressed in Chapter 4 via multi-modal techniques.

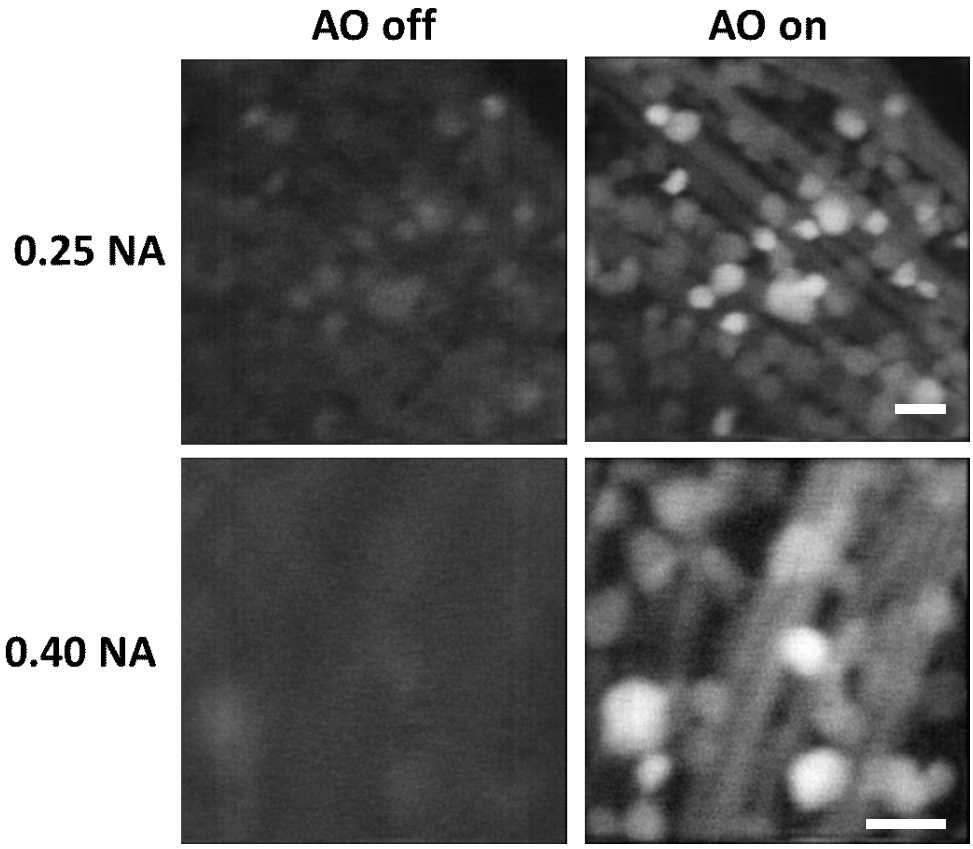

Figure 3. 9. In *vivo* Two Photon Excited Fluorescence (TPEF) images of the nerve fibre layer (NFL) of a transgenic YFP-labelled mice taken before (left column) and after (right column) images guided Sensorless Adaptive Optics (SAO), with an objective lens numerical aperture (NA) of 0.25 (top row) and 0.40 (bottom row). Scale bars: 20 µm.

3.4. Discussion

In this chapter, we presented the optical design of the SAO OCT and TPEF ocular imaging system, including simulations of various parameter adjustments, and some initial imaging results. The system is capable of capturing simultaneous volumetric OCT data and TPEF SLO images with the aid of SAO optimization. It utilizes lens-based optical relays between the deformable elements in order to map the conjugate planes to each of the VFL, DM, and GM. Following difficulties to raise the NA of the system, we modelled the optical design in the ray-tracing simulation software, Zemax Optic Studio. The results from this simulation highlighted a key issue of the design which prevented

adequate images, as well as confirmed the system's ability to correct for the increased aberrations which arise from an increased NA. Once implemented, the improvements allowed for imaging of the sensory neurons in the NFL of a YFP-labelled mouse at halved power, with slightly improved SNR despite lower average intensity.

The simulation utilized standard lenses from the Thorlabs lens catalogue, as well as models of the VFL and the mouse eye. The VFL model well represented the behavior of the device, and the mouse eye model allowed for a rough estimation of the expected imaging results. Most importantly, it demonstrated that subject to a higher NA, the VFL did not provide enough vergence to focus the beam on the features of interest around the inner retina (Figure 3.3). Because we did not require the negative focusing power which the VFL provides, we preceded the element with an achromatic lens to effectively shift its focal range to contain only positive values. We also used the simulation to model the aberrations of the system, which ensured that the majority of the aberrations originate from the mouse eye. As well as this, the aberrations introduced from the increased NA were calculated to be theoretically correctable by the DM to allow for near diffraction limited imaging conditions. It should, however, be noted that this mouse eye model shows a decided lack of higher order aberrations which are sure to be present in a real eye [51]. Despite this, spherical aberration still makes up the majority, and as such should be correctable by the DM.

With the simulated adjustments to the system implemented, we were able to image the axons and ganglion cells in the NFL of a YFP-labelled mouse. The increased vergence of the VFL allowed the focal spot to be shifted to this desired plane, and images of similar quality were achieved at half power (Figure 3.7). It unfortunately displayed poor registration results, with the edges of the features being more blurred than the previous image. This occurrence was relatively common for the TPEF images due to each frame being too dim for the registration algorithm to reliable align the frames. As we will see in Chapter 4, this can be remedied by capitalizing on the OCT signal of the bimodal imaging system.

3.5. Summary

In conclusion, we have demonstrated how our findings from simulating our SAO OCT and TPEF ophthalmoscope have influenced design choices, and ultimately allowed

for the visualization of sensory neurons at lower power. While the results were promising, poor registration of the TPEF frames resulted in images with unrealized potential. This was planned to be remedied through aid from the system's second modality, OCT, for improved motion correction as will be discussed in the next chapter.

Chapter 4.

Multi-modal imaging for low-power TPEF imaging

4.1. Introduction

Implementing TPEF imaging in a clinical setting could potentially allow for detection of earlier signs of disease that the current gold standard [35,52]. In particular, measuring autofluorescence from the Retinal Pigment Epithelium (RPE) shows potential for investigating retinal degenerative diseases such as Age-Related Macular Degeneration (AMD) and Stargardt disease [2,20,53]. Because of its innate rejection of out-of-focus light as well as its use of near infrared (NIR) light, TPEF experiences superior axial sectioning and reduced scattering throughout the optical path when compared to single photon fluorescence [22,54].

The difficulty from TPEF imaging arises mostly from its need for very high energies to trigger two-photon events. Because we are imaging *in vivo*, in order to remain non-invasive, minimizing incident exposure is required. This means that parameters outside of average power must be optimized, such as raising the instantaneous power, and minimizing the focal spot size [49,55]. The former translates to using a femtosecond pulsed laser with a low repetition rate, and the latter requires a high numerical aperture (NA).

The increased NA introduces optical aberrations which must be corrected to maintain diffraction limited imaging conditions. Adaptive Optics (AO) is a common tool to correct for these optical aberrations [2,30,32,56]. While the typical method is to use a wavefront sensor (WFS) to directly measure the ocular aberrations, this method proves difficult in the mouse eye, and as such, we utilize a sensorless AO (SAO) algorithm which avoids these difficulties [3,33].

In addition to these techniques, utilizing OCT as a second modality in conjunction with the TPEF SLO, aids to both apply initial SAO corrections, and to register the datasets. Because TPEF is a multi-photon process, the individual TPEF frames can be significantly more dim than the OCT signal which is a single photon process relying on back scattered light. As such, this imaging workflow is greatly aided by the multimodality of the system because the OCT en face images can be utilized for the initial aberration

corrections. For the same reasons, initial alignment and retinal layer selection is facilitated solely by the bright OCT signal which provides structural information throughout the full thickness of the retina. Lastly, because the acquisition of the two modalities is synchronized, we are able to register the OCT signal, and use this transformation data to correct the motion in the TPEF data before averaging.

In this chapter, we present on our imaging system that uses SAO and OCT to allow for high resolution TPEF images of retinal features, at powers below ANSI maximum permissible exposure limits. In order to correct for the motion of the *in vivo* sample, we utilize the feature rich OCT data in order to register the TPEF frames before averaging, which allowed for lower powers than previously attained. We demonstrated this technique on YFP-labelled retinal ganglion cells within the nerve fibre layer (NFL) of a pigmented mouse, as well as in the RPE layer of a mouse displaying advanced retinal degeneration.

4.2. Methods

An updated schematic of the optical design is shown in Figure 4.1. The majority of the components remain the same as in Section 3.2.2, and described here is a compilation of the system changes. A pre-chirp pulse compressor for dispersion compensation was designed and aligned ex-situ, but not implemented into the system. The compressor was calculated to reduce the pulse width of our source light from ~120 to ~90 fs, which from Equation 2.4 shows an approximately 30% signal increase. Because the potential signal improvement from raising the NA is significantly higher, this was prioritized. The next change to the system was the 200 mm achromat preceding the VFL, in order to increase its vergence to allow the system to focus on the inner retina. This shifted the optical power of the VFL from -5 to 15 diopters, to 0 to 20 diopters. Last, are the changes to the final relay and the TPEF detection path. Because of potential signal loss due to clipping on the galvanometer mirrors, the fluorescent light was reflected by a dichroic mirror placed between the final relay lenses. This light was then focused into the PMT using a 60 mm lens. As for the final relay, these lenses were changed to a 2x100 mm compound lens and a 30 mm lens to reduce the demagnification of the beam, and raise the NA from 0.25 to 0.4.

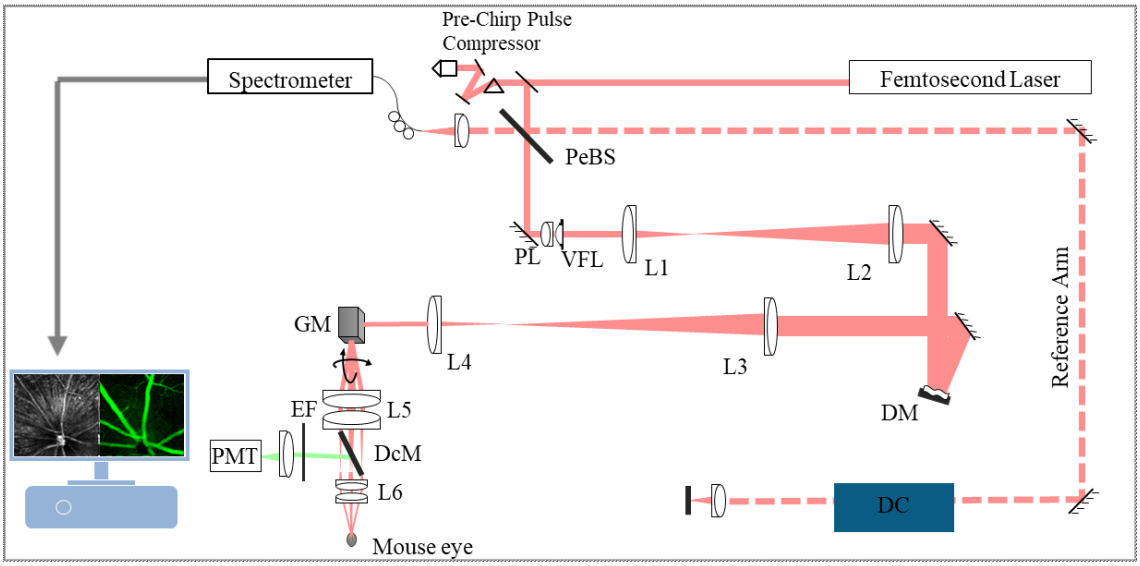

Figure 4. 1. Schematic of the SAO OCT and TPEF imaging system. The imaging system was constructed with pre-chirp pulse compressor, a pellicle beam splitter (PeBS), variable focus lens (VFL) preceded by 200mm lense (PL), deformable mirror (DM), dichroic mirror (DcM), galvanometer-scanning mirrors (GM), emission filters (EF), photo-multiplier tube (PMT), dispersion compensation (DC), and the following lenses: L1=100 mm, L2=300 mm, L3=400 mm, L4=100 mm, L5=2x125 mm, L6=2x50 mm. The reference arm denoted as a dashed line.

While the bulk of the image processing for our TPEF acquisitions is the same as the previous section, that of the OCT volumes required a slightly different approach. As well as this, for our low power imaging, we will see that the TPEF is registered using solely the OCT transformation data rather than its own. Because this method utilizes multiple OCT volumes, the first step is to apply motion correction in the *z*-direction such that the maximum intensity projections (MIP's) section out the same depths. This is accomplished by computing the cross-correlation between the first and each subsequent volume, then circularly shifting the matrix in the *z*-direction such that the cross-correlation is maximized. Here, a phantom comprised of simple lens paper was used to provide a mostly flat structure which maintains visible structure in the *en face* images. 100 OCT volumes were acquired while motion was introduced via a three-dimensional

linear stage to simulate motion from an *in vivo* sample. This motion can be seen in Figure 4.2 where before correction, there is a clear vertical shift between the two volumes where magenta shows the target frame, and green the reference frame. This discrepancy between the two volumes would cause the MIP's to project different sample depths. After the shift, the volumes align, which allows for manual selection of the layers of interest, and thus an *en face* image ready for registration.

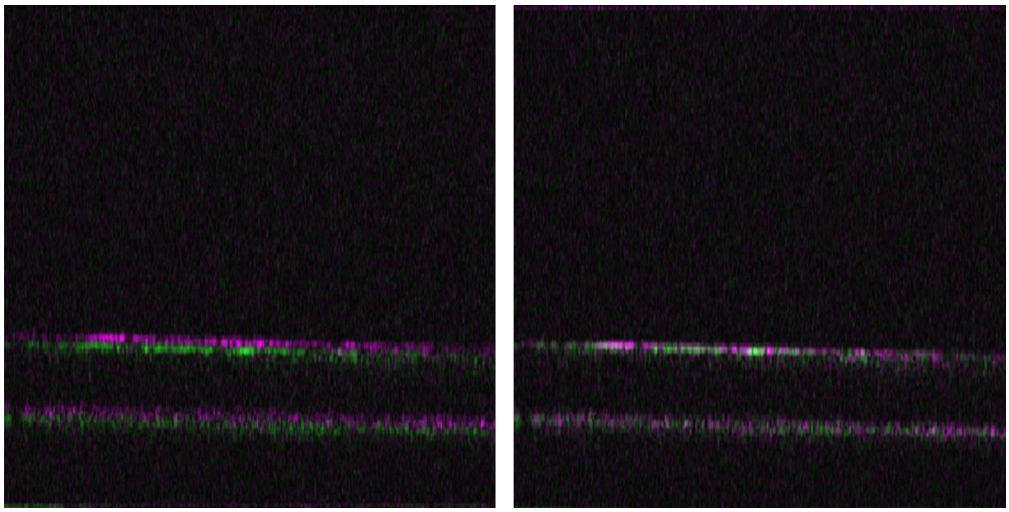

Figure 4. 2. A comparison of OCT B-scans from 2 separate volumes acquired 6 seconds apart, where magenta shows the target frame, and green the reference. Left shows before cross-correlation based motion correction, and right after.

The registration of the *en face* projections utilized the Medical Image Registration Toolbox (MIRT) [50], as in Section 3.3.2. MIRT non-rigidly registers each image to the chosen target image using cubic B-spline based transformation parametrization. The toolbox allows for control of various parameters such that it can be applicable to a wide range of medical imaging applications. Most of the parameters were left at their recommended defaults, though a handful were adjusted for best performance. These parameters included the similarity metric, the mesh window size between the B-spline control points, and the regularization weight. The similarity metric was chosen to be an ultrasound specific similarity metric developed by B. Cohen and I. Dinstein which qualitatively produced the most accurate results, likely due to the similar speckle present in both techniques [57]. The mesh windows size and regularization weights were adjusted iteratively until we saw adequate registration results with minimal overfitting. By reducing the mesh window size, more subtle motion could be corrected, but this

introduced overfitting errors. This would be counteracted by both increasing the regularization weight and increasing the image smoothing via a Weiner filter before registration. The former would act to lessen the displacements of the B-spline control points, and the latter to minimize fitting to the speckle noise. Finally, the algorithm outputs a transformation matrix corresponding to each frame, which would be applied to the unfiltered set of OCT MIP *en face* images.

Because the OCT and TPEF data is acquired simultaneously pixel by pixel, the motion is between frames is consistent between the two modalities. This can be seen in Figure 4.3, where a displacement field was taken between a target and reference frame for both TPEF and OCT. Below the fields are overlays of the corresponding frames where magenta shows the target frame, and green the reference. While there are discrepancies on the right side of the displacement fields arising from lack of signal, where there is adequate signal, the fields match well. This transformation matrix can be applied to the TPEF frames to register both modalities while having only processed the one. As we will see in Section 4.3, this is especially useful when the TPEF frames contain significantly less signal than the OCT. Because TPEF is a multi-photon process, whilst OCT is a single photon process relying on back reflection, at low powers, the OCT has significantly higher SNR making it a better candidate for registration.

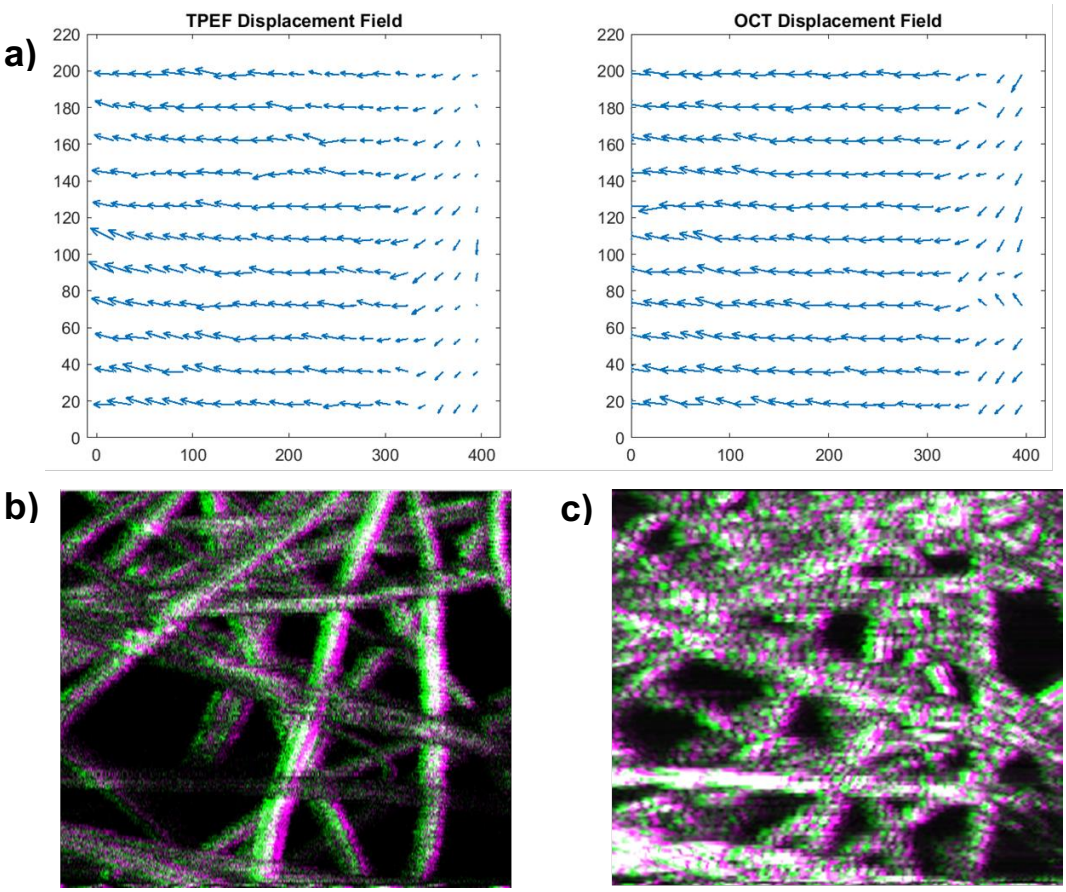

Figure 4. 3. A comparison of TPEF and OCT displacement fields between the target and reference frame (a), demonstrating their shared motion. Below are overlays of the corresponding frames where magenta shows the target frame, and green the reference, for both TPEF (b) and OCT (c).

A demonstration of the algorithm's final result is shown in Figure 4.4, where 100 OCT volumes were acquired alongside the TPEF frames. Top shows an intensity line plot of each between the arrows, left shows the averaged image of all 100 TPEF frames, middle that of the registered set where OCT was used as the registration reference, and right that with the TPEF as the reference. The unregistered data shows the artificial motion introduced by manually adjusting the linear stage, and the registered images demonstrate adequate motion correction. Qualitatively, the images look identical, and the structural similarity was calculated to be 0.89, indicating very high similarity between the two methods [58]. A comparison of the motion present *in vivo* versus the phantom imaging experiment is shown in Figure 4.5, where the former displays motion ~8% of the FOV, and the latter ~4%. Therefore, because of the similar magnitude of motion, when imaging conditions result in a TPEF dataset too dim to properly register, we can expect to maintain high quality motion correction by registering the OCT instead.

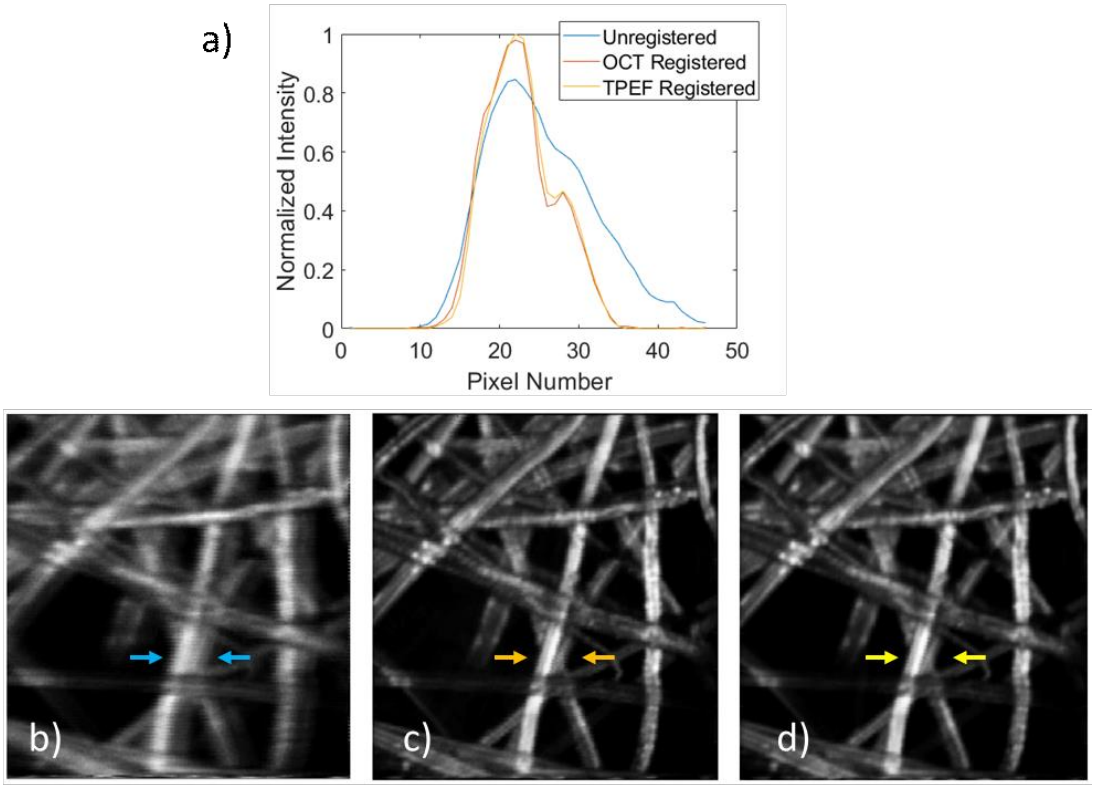

Figure 4. 4. **Averaged TPEF frames from fluorescent lens paper phantom showing an intensity line plot for each between the arrows (a), unregistered frames (b), frames registered via OCT reference (c), and frames registered via TPEF reference (d).**

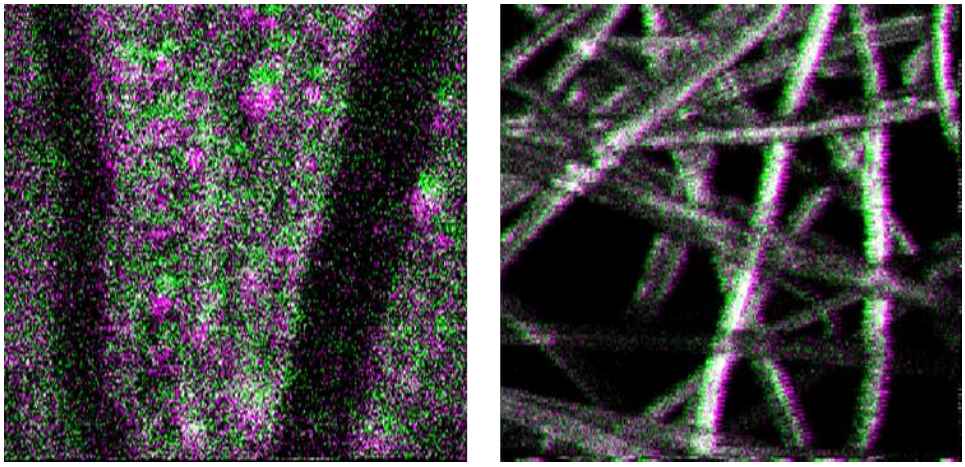

Figure 4. 5 **Comparison of motion, between single frames of TPEF from *in vivo* images from a YFP labelled mouse (left), and fluorescein-soaked lens paper (right). Average motion in the former was ~8% of the FOV, and ~4% in the latter.**

4.3. Results

The in vivo imaging results are split into two parts, the first describing the low-power imaging of the NFL, and the second presenting some preliminary results on RPE imaging. Section 4.3.1 demonstrates the use of the registration algorithm coupled with AO which allowed for visualization of YFP-labelled sensory neurons at sub milliwatt laser power. Section 4.3.2 will present two TPEF images of the RPE layer from a mouse with a RPE65 gene mutation that causes retinal degeneration.

4.3.1. AO and image registration for low power TPEF imaging

Figure 4.6 shows co-acquired TPEF and OCT images taken at 0.4 NA from the NFL of a YFP-labelled mouse of strain B6.Cg-Tg(Thy1-YFP)16Jrs/J, alongside the applied Zernike coefficients. Here, the laser was adjusted to 940 nm at 1.3 mW, and the focal plane was shifted to the NFL before AO optimizations were run using the TPEF image as the metric. The TPEF images consist of 200 frames registered and averaged separately to the OCT, which is only a single max-intensity projection of the NFL, where the projection boundaries were chosen by hand. The top left panel demonstrates the performance in the absence of SAO, and top right panel after the fact. Both modalities see an improvement of signal intensity of ~20 percent where the improvement was calculated by comparing the sum of the pixels before and after SAO optimization.

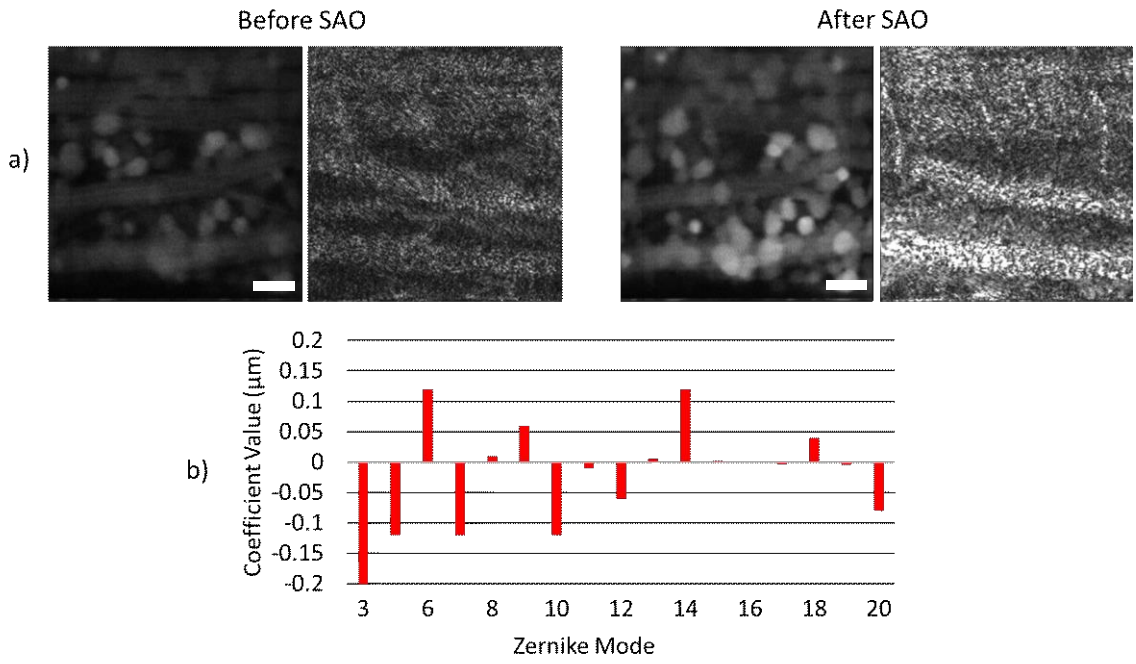

Figure 4. 6. (a) In *vivo* Two Photon Excited Fluorescence (TPEF) and Optical Coherence Tomography (OCT) *en face* images of the nerve fiber layer (NFL) of a transgenic YFP-labelled mouse taken at 0.4 NA, before and after image guided Sensorless Adaptive Optics (SAO). (b) Zernike coefficients applied to the deformable mirror. Scale bars: 20 µm.

Utilizing these methods, we were able to halve the laser powers to 0.625 mW without sacrificing much structural content in the image (Figure 4.7). Here, the laser powers are within the ANSI maximum permissible exposure limits. Though the limits for ultrashort laser pulses are ill-defined within these guidelines, recent work shows no apparent damage when utilizes these laser classifications in macaque eyes [52]. By lowering the laser power by half, the sum of pixel intensity lowered by 4.71 times, where we expect from theory a dimming of 4 times. This small discrepancy is likely due to digitization and image thresholding which occurs pre-processing.

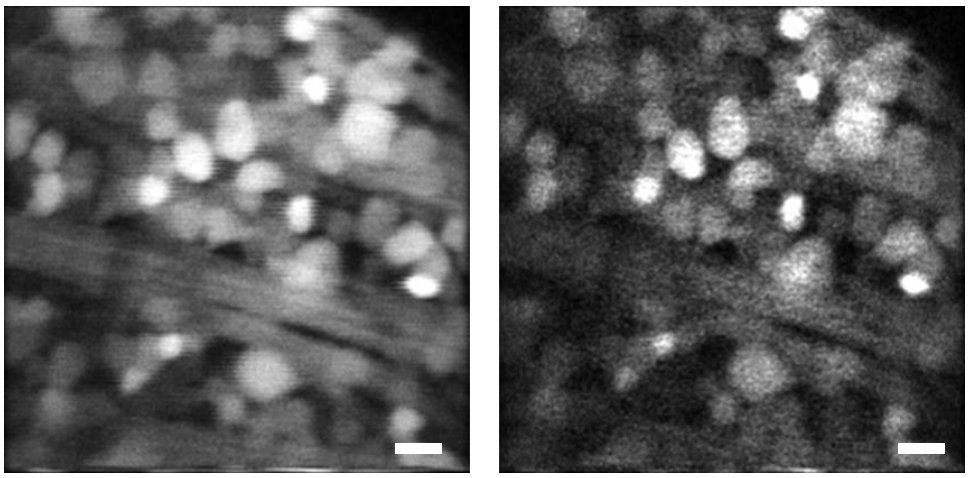

Figure 4. 7. In *vivo* Two Photon Excited Fluorescence (TPEF) *en face* images of the nerve fiber layer (NFL) of a transgenic YFP-labelled mouse taken at 0.4 NA, with 1.3 mW incident laser power (left) and 0.625 mw (right). Scale bars: 20 μm.

While these results are promising, the overarching goal of this project is to image endogenous fluorophores of the eye, which exhibit significantly lower quantum efficiency than YFP. Because of this, we investigated the efficacy of the co-registration algorithm under these *in vivo* imaging conditions. We began with incident power of 1.3 mW to confirm expected behaviours compared to the phantom measurements. Figure 4.8 shows these results, with the top showing a single frame of TPEF alongside a maximum intensity projection (MIPs) of the same layer from the corresponding OCT volume. Here, it's clear that both the TPEF and OCT *en face* images have adequate features for registration. This is confirmed by the bottom three images where from left to right is the averaged 100 TPEF frames from the unregistered data set, the set registered via OCT reference, and that registered via TPEF reference. Here, the structural similarity was calculated to be 0.74, which demonstrates slightly worse correlation than in the phantom data. Despite this, both modalities provided adequate registration results which demonstrates the technique's viability for *in vivo* imaging. Figure 4.9 from left to right shows the averaged 100 OCT MIPs, their corresponding averaged TPEF frames, and their overlayed images, with both datasets registered using the OCT as reference.

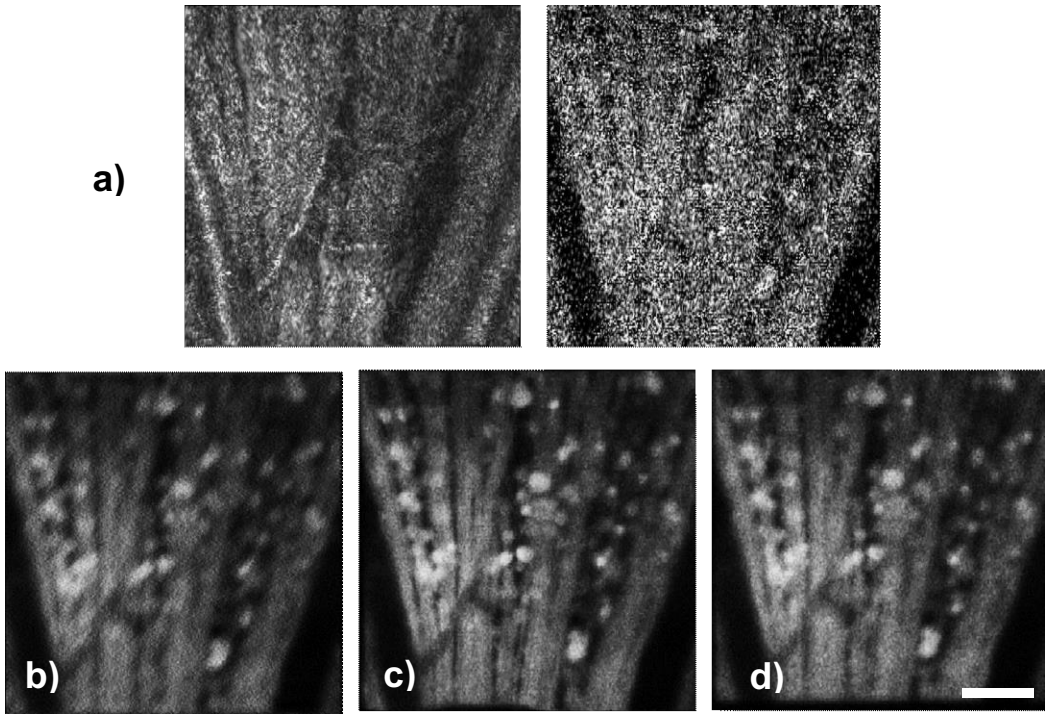

Figure 4. 8. In *vivo* TPEF and OCT *en face* images of the nerve fiber layer (NFL) of a transgenic YFP-labelled mouse taken at 1.3 mW incident laser power and 0.4 NA. Shown is a single frame of TPEF and a maximum intensity projection of the same layer from the corresponding OCT volume (a), and then the average of 100 unregistered frames (b), frames registered via OCT reference (c), and frames registered via TPEF reference (d). Scale bar: 100 µm.

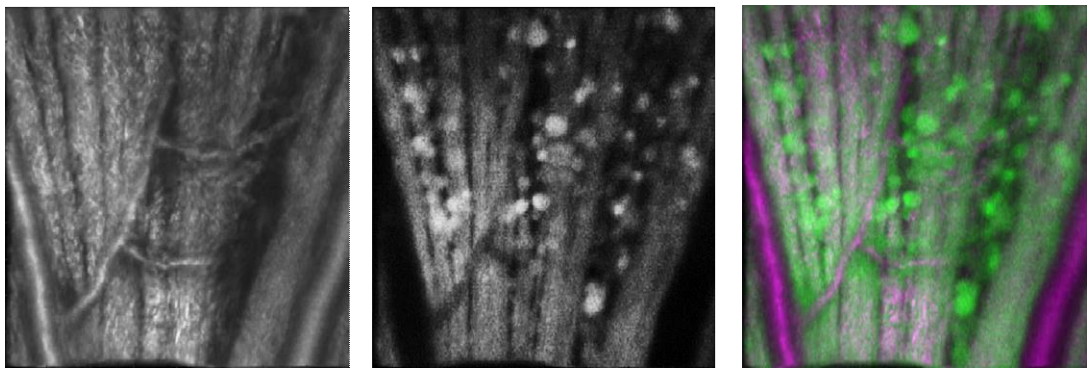

Figure 4. 9. In *vivo* TPEF and OCT *en face* images of the nerve fiber layer (NFL) of a transgenic YFP-labelled mouse taken at 1.3 mW incident laser power and 0.4 NA. Shown are 100 averaged maximum intensity projections (MIPs) from the OCT volumes (left), 100 averaged co-acquired TPEF frames (middle), and their overlayed image (right). Both datasets were registered using the OCT MIPs as reference.

With the registration algorithm working as expected, we acquired another data set at 0.625 mW, and with the PMT gain lowered. At this lowered power, the individual TPEF frames were still bright enough to register due to the YFP molecules being so highly fluorescent. Because this power is within the maximum permissible exposure limits, rather than further lower the power, we chose to lower the PMT gain to simulate a fluorophore of low quantum efficiency. This allowed us to maintain the expected OCT signal, whilst lowering the detected fluorescent signal in order to more closely model the techniques intended use. Figure 4.10 shows the result of this in the same format as Figure 4.8. Here, a single frame of TPEF displays significantly less features than the corresponding OCT MIP. By registering the OCT rather than the TPEF, the registration yields decidedly better results.

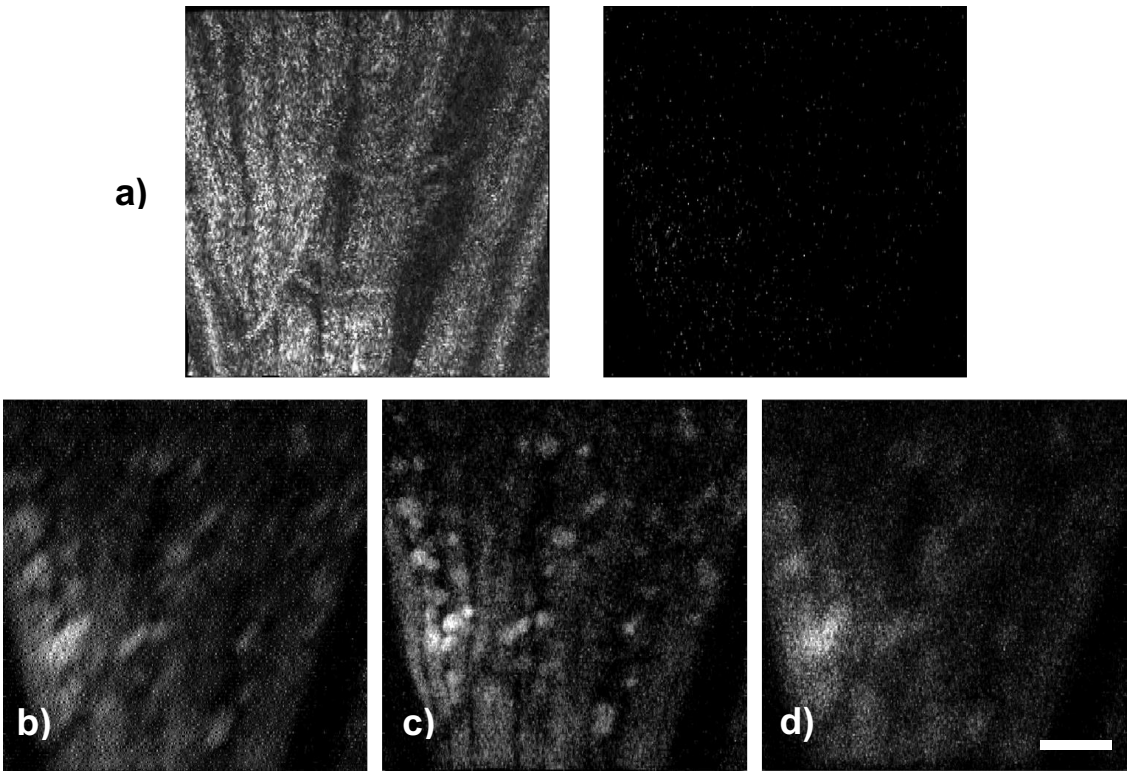

Figure 4. 10. In *vivo* Two Photon Excited Fluorescence (TPEF) and OCT *en face* images of the nerve fiber layer (NFL) of a transgenic YFP-labelled mouse taken at 0.625 mW incident laser power and 0.4 NA, with low PMT gain. Shown is a single frame of TPEF and a maximum intensity projection of the same layer from the corresponding OCT volume (a), and then the average of 100 unregistered frames (b), frames registered via OCT reference (c), and frames registered via TPEF reference (d). Scale bar: 100 µm.

4.3.2. RPE imaging

TPEF images of the RPE layer were acquired from a pigmented mouse with a disruption of the rpe65 gene (B6(A)-RPE65^{rd12}/J) which causes retinal degeneration. A set of 900 TPEF frames was acquired at 1.2 mW and 0.4 NA with a center wavelength of 740 nm, and Figure 4.11 shows an average of the frames both before (left) and after motion correction (right). This registration was guided by the TPEF frames, shows similar results as in Section 4.3.1, where little improvement can be seen due a lack of features in individual frames. The hexagonal structure of the cells can nearly be visualized, despite imaging with ~8 times less power than in our previous work [12]. As well as this, because the mouse is pigmented, much of the excitation and emission light is absorbed. The concentrated areas of increased fluorescence are likely due to retinyl ester storage particles arising from cell degeneration [40,41].

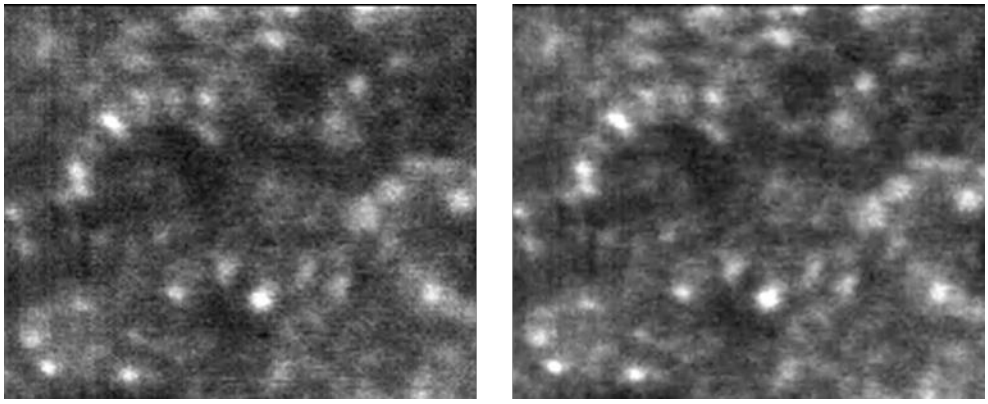

Figure 4. 11. Averaged TPEF images from the RPE of a mouse before (left) and after (right) TPEF guided motion correction, comprising of 900 frames. 1.2 mW of laser power was used at 0.4 NA.

Our registration method was then applied, where 100 OCT volumes were acquired alongside 100 TPEF frames at 2.7 mW. From left to right, Figure 4.12 shows an average of these 100 frames without motion correction, with TPEF guided motion correction, and OCT guided. Because of the increased acquisition time of the OCT, the images suffer from reduced SNR due to fewer frames. This is clear when comparing the unregistered data from Figures 4.11 and 4.12, where the latter's features are much less

pronounced. While the TPEF guided registration provided improved motion correction due to the increased power, the results remain sub-par. The OCT guided registration provided significantly better results, with the build-up of the retinyl ester storage particles beginning to contrast with the background. The hexagonal structure is nearly visible, but more frames are needed to properly visualize the mosaic.

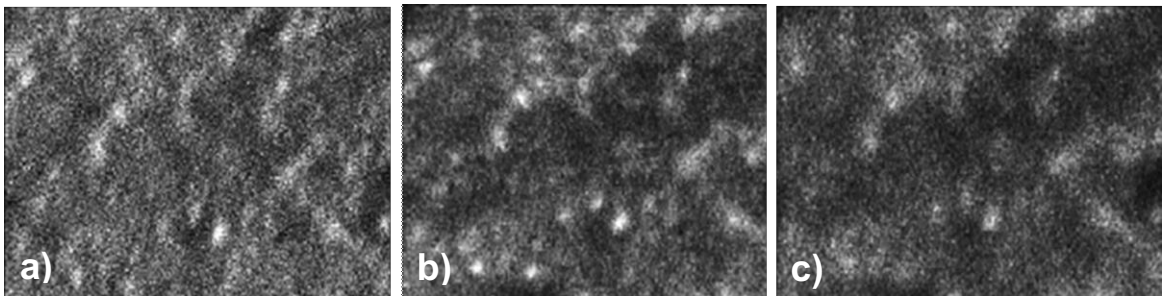

Figure 4. 12. Averages of 100 TPEF images from the RPE layer of a mouse before motion correction (a), after OCT guided motion correction (b), and after TPEF guided motion correction (c). 2.7 mW of laser power was used at 0.4 NA.

4.4. Discussion

In this chapter, we presented imaging results from our SAO TPEF and OCT ophthalmoscope, as well as an algorithm which capitalized on the system's multi-modality to facilitate low power imaging. When imaging light sensitive tissue such as the retina, incident power must be kept low to avoid damage. Because of this, parameters excluding the power must be maximized to acquire adequate images. The most important amongst these is the NA due to its quartic relationship with TPEF efficiency. With high NA, however, monochromatic aberrations are introduced which distort the focal spot, ultimately discounting these benefits. To correct for this, we used sensorless adaptive optics to distort the wavefront with the inverse of these aberrations, thus providing near diffraction limited performance. In conjunction with these methods, to maintain these low incident laser powers, we conducted image acquisitions over long time periods to average many frames of data. While this is a simple process for a static

sample, for *in vivo* imaging, breathing introduces motion between frames which must be corrected. Because each individual TPEF frame was so dim, there was commonly not sufficient signal for registration algorithms to correct for the motion. To remedy this, we utilized the system's second modality of OCT to register the data set. Because OCT signal scales linearly rather than square with incident power, at low powers, it contains significantly more features than TPEF. These two modalities are acquired concurrently, so by registering the OCT, we were able to apply the same transformations to the TPEF to achieve superior results to natively registering the TPEF frames.

The results from this algorithm allowed for sub-milliwatt laser powers, which has been shown to likely be safe for use on humans [37,52]. The co-registration shows clear improvement over natively registering the TPEF frames, especially for fluorophores of low quantum efficiency. In these cases, without the OCT, we were not able to correct for the motion, which shows promise for future use of the technique. The goal of the system is to be used in a clinical setting, where intrinsic fluorophores, such as those found in the RPE layer, will be targeted. These fluorophores demonstrate very low quantum efficiency much like in our experiments, and as such could benefit from this co-acquisition. One drawback is the acquisition time which is gated by the OCT. Our results indicate that it is expected to take 500 to 900 TPEF frames in order to achieve adequate signal from the RPE. At ~1 volume per second, this results in acquisition times of 8 to 15 minutes, with several GB of data for a single image. Ideally, the images could be constructed with fewer frames to allow for more realistic acquisition times. Recent work from Palczewska *et al* has employed the use of ultra-short laser pulses between 20 and 75 femtoseconds in order to further lower laser powers [36,55]. As well as this, they have used pulse picking devices to lower their repetition rate from 80 to 8 MHz. This allowed for higher peak power whilst maintaining their average power, which increased signal without causing thermal damage to the tissue. They utilized these techniques to acquire TPEF fundus images on human subjects, where they found similarities between human and mouse models of retinal diseases [59]. While for this work, we were unable to reduce pulse width due to widening of spectral bandwidth, lower repetition rate in conjunction with our multi-modal approach could allow for faster acquisitions without sacrificing image quality.

Chapter 5.

Future work and conclusion

5.1. Technology Advancement

Implementation of emerging technologies for two photon imaging in the retina is essential for the progression of the technique to human imaging. While the results presented in this thesis are encouraging, the advancement to human imaging presents a number of challenges.

The most significant hurdle is that of maintaining eye safe laser exposure. While the powers used in this thesis have been shown to incur no damage, the human eye is only capable for NA approximately half that of a mouse. As such, further improvement to TPEF efficiency must be developed. As previously mentioned, significant improvements have been demonstrated by using a lower laser repetition rate with a higher peak power. Because TPEF efficiency scales with the square of the power, by raising peak energy, it is possible to increase the acquired signal whilst maintaining low average power. In addition to this, by increasing OCT acquisition speed, the co-registration method would be able to acquire a large number of frames without excessive integration times. Recent work by Dr. Miao *et al* has demonstrated a dual-spectrometer OCT system where two spectrometers are operated such that the trigger signals of each are π shifted out of phase with each other [60,61]. This allows for each camera to acquire during the other's dead time, thus allowing for a 500 kHz A-line scan rate, which is twice as fast as the maximum speed of a single line-scan camera. This method coupled with lower pulse repetition rate would allow for lower laser exposure, and progress the technique further towards human imaging.

5.2. Fluorescent Lifetime Microscopy

When imaging intrinsic fluorophores in the retina, such as in the RPE layer, the signal is often comprised from the fluorescence of many different molecules. By employing a technique known as fluorescent lifetime imaging microscopy (FLIM), contrast can be created between these fluorophores of similar emission spectra by measuring fluorescence decay rate [62,63]. This allows one's signal to be mostly

independent of fluorophore concentration, and gives the ability to distinguish between many fluorophores occupying a small area. It also has been shown to provide insight into the health of the cells within the retina. FLIM has been demonstrated both in mouse and mammalian eye, and its combination with TPEF SLO shows potential in detecting retinal diseases before structural damage occurs [36,55,63,64]. While there are many methods for conducting FLIM, time-correlated single photon counting lends itself well to TPEF imaging systems such as ours due to its need for ultra-short pulsed lasers and photomultiplier tubes. Because of this, all that would be required is time-amplitude converter electronics.

5.3. Conclusion

Imaging the mouse retina via fluorescence can provide a means of modelling progression of retinal degeneration, which could be used to develop therapies for vision robbing diseases. This technique, however, presents difficulties pertaining to the size of the focal spot, and limits on incident laser power. The work in this thesis involved continued work on resolving these issues through improvement of optical design and the use of registration software to allow for low power imaging.

The resulting system was a multi-modal Optical Coherence Tomography (OCT) and Two-Photon Excited Fluorescence (TPEF) Scanning Laser Ophthalmoscope (SLO). In order to increase TPEF efficiency, the numerical aperture (NA) of the system was increase, which introduces mono-chromatic aberrations that distort the focal spot. This was counteracted through the use of Sensorless Adaptive Optics (SAO) to allow for near diffraction limited imaging. When reducing the laser power to eye-safe levels, the resulting TPEF images were too dim to reliably register, so we capitalized on the co-acquisition of the system by registering maximum intensity projections (MIPs) from the OCT, and applying the transformations to the TPEF images. The technique was successful and allowed for motion correction where not possible without the second modality. By increasing acquisition speed of the OCT, autofluorescence of the RPE mosaic will be attainable through reasonable acquisition times.

References

1. "Blindness In Canada," https://www.cnib.ca/en/sight-loss-info/blindness/blindness-canada?region=bc.
2. S. Marcos, J. S. Werner, S. A. Burns, W. H. Merigan, P. Artal, D. A. Atchison, K. M. Hampson, R. Legras, L. Lundstrom, G. Yoon, J. Carroll, S. S. Choi, N. Doble, A. M. Dubis, A. Dubra, A. Elsner, R. Jonnal, D. T. Miller, M. Paques, H. E. Smithson, L. K. Young, Y. Zhang, M. Campbell, J. Hunter, A. Metha, G. Palczewska, J. Schallek, and L. C. Sincich, "Vision science and adaptive optics, the state of the field," Vision Res. **132**, 3–33 (2017).
3. Y. Geng, L. A. Schery, R. Sharma, A. Dubra, K. Ahmad, R. T. Libby, and D. R. Williams, "Optical properties of the mouse eye," Biomed. Opt. Express **2**(4), 717 (2011).
4. J. M. Skeie, S. H. Tsang, and V. B. Mahajan, "Evisceration of mouse vitreous and retina for proteomic analyses," J. Vis. Exp. (50), 2795 (2011).
5. N. Mahabadi and Y. Al Khalili, *Neuroanatomy, Retina* (StatPearls Publishing, 2022).
6. S. L. S. Ding, S. Kumar, and P. L. Mok, "Cellular Reparative Mechanisms of Mesenchymal Stem Cells for Retinal Diseases," Int. J. Mol. Sci. **18**(8), (2017).
7. R. K. Crouch, "The Visual Cycle," http://photobiology.info/Crouch.html.
8. D. Darling, "Adaptive Optics," https://www.daviddarling.info/encyclopedia/A/adaptive_optics.html.
9. M. Konnik and J. Dona, "Waffle mode mitigation in adaptive optics systems: A constrained Receding Horizon Control approach," in *Proceedings of the American Control Conference* (2013).
10. V. Akondi and A. Dubra, "Multi-layer Shack-Hartmann wavefront sensing in the point source regime," Biomed. Opt. Express **12**, 409 (2021).
11. M. J. Ju, M. Heisler, D. Wahl, Y. Jian, and M. V. Sarunic, "Multiscale sensorless adaptive optics OCT angiography system for in vivo human retinal imaging," J. Biomed. Opt. **22**(12), 1 (2017).
12. D. J. Wahl, M. J. Ju, Y. Jian, and M. V. Sarunic, "Non-invasive cellular-resolution retinal imaging with two-photon excited fluorescence," Biomed. Opt. Express **10**(9), 4859 (2019).
13. W. Newberry, D. J. Wahl, M. J. Ju, Y. Jian, and M. V Sarunic, "Progress on Multimodal Adaptive Optics OCT and Multiphoton Imaging," in *2020 IEEE Photonics Conference (IPC)* (2020), pp. 1–2.
14. W. B. Newberry and M. V Sarunic, "Progress on Multimodal Retinal Imaging via OCT and Two Photon Excited Fluorescence," in *European Conferences on Biomedical Optics 2021 (ECBO)* (Optica Publishing Group, 2021), p. ETu1D.5.
15. W. Newberry, L. Vargas, and M. V Sarunic, "Progress on Bimodal Adaptive Optics OCT and Two-Photon Imaging," in *2021 IEEE Photonics Conference (IPC)* (2021), pp. 1–2.

16. W. Newberry, L. Vargas, and M. V Sarunic, "Progress on multimodal retinal Imaging via OCT multi-volume averaging and two photon excited fluorescence," in *Optical Coherence Tomography and Coherence Domain Optical Methods in Biomedicine XXVI*, J. A. Izatt and J. G. Fujimoto, eds. (SPIE, 2022), **PC11948**, p. PC119480G.

17. M. Cua, D. J. Wahl, Y. Zhao, S. Lee, S. Bonora, R. J. Zawadzki, Y. Jian, and M. V. Sarunic, "Coherence-Gated Sensorless Adaptive Optics Multiphoton Retinal Imaging," Sci. Rep. **6**(1), 32223 (2016).

18. R. H. Webb and G. W. Hughes, "Scanning laser ophthalmoscope.," IEEE Trans. Biomed. Eng. **28**(7), 488–492 (1981).

19. T. Liu, H. Jung, J. Liu, M. Droettboom, and J. Tam, "Noninvasive near infrared autofluorescence imaging of retinal pigment epithelial cells in the human retina using adaptive optics.," Biomed. Opt. Express **8**(10), 4348–4360 (2017).

20. L. L. Molday, D. Wahl, M. V Sarunic, and R. S. Molday, "Localization and functional characterization of the p.Asn965Ser (N965S) ABCA4 variant in mice reveal pathogenic mechanisms underlying Stargardt macular degeneration," Hum. Mol. Genet. **27**(2), 295–306 (2018).

21. U. Kellner, S. Kellner, B. H. F. Weber, B. Fiebig, S. Weinitz, and K. Ruether, "Lipofuscin- and melanin-related fundus autofluorescence visualize different retinal pigment epithelial alterations in patients with retinitis pigmentosa.," Eye (Lond). **23**(6), 1349–1359 (2009).

22. W. Denk, J. Strickler, and W. Webb, "Two-photon laser scanning fluorescence microscopy," Science **248**(4951), 73–76 (1990).

23. D. R. Williams, "Imaging single cells in the living retina," Vision Res. **51**(13), 1379–1396 (2011).

24. Y. Jian, S. Lee, M. J. Ju, M. Heisler, W. Ding, R. J. Zawadzki, S. Bonora, and M. V Sarunic, "Lens-based wavefront sensorless adaptive optics swept source OCT," Sci. Rep. **6**(1), 27620 (2016).

25. E. Dalimier and C. Dainty, "Comparative analysis of deformable mirrors for ocular adaptive optics," Opt. Express **13**(11), 4275–4285 (2005).

26. A. Roorda, F. Romero-Borja, I. Donnelly, H. Queener, T. Hebert, and M. Campbell, "Adaptive optics scanning laser ophthalmoscopy," Opt. Express **10**(9), 405–412 (2002).

27. R. J. Zawadzki, S. M. Jones, S. S. Olivier, M. Zhao, B. A. Bower, J. A. Izatt, S. Choi, S. Laut, and J. S. Werner, "Adaptive-optics optical coherence tomography for high-resolution and high-speed 3D retinal in vivo imaging," Opt. Express **13**(21), 8532 (2005).

28. D. T. Miller, J. Qu, R. S. Jonnal, and K. E. Thorn, "Coherence gating and adaptive optics in the eye," in *Coherence Domain Optical Methods and Optical Coherence Tomography in Biomedicine VII*, V. V Tuchin, J. A. Izatt, and J. G. Fujimoto, eds. (SPIE, 2003), **4956**, pp. 65–72.

29. V. N. Mahajan and S. of Photo-optical Instrumentation Engineers, *Aberration Theory Made Simple*, SPIE Tutorial Texts (SPIE Optical Engineering Press, 1991).

30. J. Porter, H. Queener, J. Lin, K. Thorn, and A. Awwal, *Adaptive Optics for Vision Science: Principles, Practices, Design and Applications* (Wiley, 2006).

31. S. N. Bezdidko, "The Use of Zernike Polynomials in Optics," Sov. J. Opt. Techn. **41**(425), (1974).

32. Y. Geng, A. Dubra, L. Yin, W. H. Merigan, R. Sharma, R. T. Libby, and D. R. Williams, "Adaptive optics retinal imaging in the living mouse eye," Biomed. Opt. Express **3**(4), 715–734 (2012).

33. D. J. Wahl, P. Zhang, J. Mocci, M. Quintavalla, R. Muradore, Y. Jian, S. Bonora, M. V. Sarunic, and R. J. Zawadzki, "Adaptive optics in the mouse eye: wavefront sensing based vs image-guided aberration correction," Biomed. Opt. Express **10**(9), 4757 (2019).

34. A. J. Bower, T. Liu, N. Aguilera, J. Li, J. Liu, R. Lu, J. P. Giannini, L. A. Huryn, A. Dubra, Z. Liu, D. X. Hammer, and J. Tam, "Integrating adaptive optics-SLO and OCT for multimodal visualization of the human retinal pigment epithelial mosaic," Biomed. Opt. Express **12**(3), 1449 (2021).

35. D. J. Wahl, R. Ng, M. J. Ju, Y. Jian, and M. V. Sarunic, "Sensorless adaptive optics multimodal en-face small animal retinal imaging," Biomed. Opt. Express **10**(1), 252–267 (2019).

36. G. Palczewska, P. Stremplewski, S. Suh, N. Alexander, D. Salom, Z. Dong, D. Ruminski, E. H. Choi, A. E. Sears, T. S. Kern, M. Wojtkowski, and K. Palczewski, "Two-photon imaging of the mammalian retina with ultrafast pulsing laser.," JCI insight **3**(17), 121555 (2018).

37. C. Schwarz, R. Sharma, S. K. Cheong, M. Keller, D. R. Williams, and J. J. Hunter, "Selective S Cone Damage and Retinal Remodeling Following Intense Ultrashort Pulse Laser Exposures in the Near-Infrared," Invest. Ophthalmol. Vis. Sci. **59**(15), 5973–5984 (2018).

38. R. Sharma, L. Yin, Y. Geng, W. H. Merigan, G. Palczewska, K. Palczewski, D. R. Williams, and J. J. Hunter, "In vivo two-photon imaging of the mouse retina," Biomed. Opt. Express **4**(8), 1285–1293 (2013).

39. G. Palczewska, Z. Dong, M. Golczak, J. J. Hunter, D. R. Williams, N. S. Alexander, and K. Palczewski, "Noninvasive two-photon microscopy imaging of mouse retina and retinal pigment epithelium through the pupil of the eye," Nat. Med. **20**(7), 785–789 (2014).

40. P. Stremplewski, K. Komar, K. Palczewski, M. Wojtkowski, and G. Palczewska, "Periscope for noninvasive two-photon imaging of murine retina in vivo.," Biomed. Opt. Express **6**(9), 3352–3361 (2015).

41. Y. Imanishi, M. L. Batten, D. W. Piston, W. Baehr, and K. Palczewski, "Noninvasive two-photon imaging reveals retinyl ester storage structures in the eye.," J. Cell Biol. **164**(3), 373–383 (2004).

42. W. R. Zipfel, R. M. Williams, and W. W. Webb, "Nonlinear magic: multiphoton microscopy in the biosciences," Nat. Biotechnol. **21**(11), 1369–1377 (2003).

43. Y. Jian, K. Wong, and M. V Sarunic, "Graphics processing unit accelerated optical coherence tomography processing at megahertz axial scan rate and high resolution video rate volumetric rendering," J. Biomed. Opt. **18**(2), 026002 (2013).

44. J. Xu, K. Wong, Y. Jian, and M. V Sarunic, "Real-time acquisition and display of flow contrast using speckle variance optical coherence tomography in a graphics processing unit," J. Biomed. Opt. **19**(2), 026001 (2014).

45. D. J. Wahl, Y. Jian, S. Bonora, R. J. Zawadzki, and M. V. Sarunic, "Wavefront sensorless adaptive optics fluorescence biomicroscope for in vivo retinal imaging in mice," Biomed. Opt. Express **7**(1), 1 (2016).

46. A. Facomprez, E. Beaurepaire, and D. Débarre, "Accuracy of correction in modal sensorless adaptive optics," Opt. Express **20**(3), 2598 (2012).

47. M. R. Gardner, H. G. Rylander, and T. E. Milner, "Computational Model (Zemax) of a Mouse Eye for Visible and Near-Infrared Wavelength Ranges," https://repositories.lib.utexas.edu/handle/2152/46337.

48. A. Dubra and Z. Harvey, "Registration of 2D Images from Fast Scanning Ophthalmic Instruments," in *Biomedical Image Registration*, B. Fischer, B. M. Dawant, and C. Lorenz, eds. (Springer Berlin Heidelberg, 2010), pp. 60–71.

49. N. S. Alexander, G. Palczewska, P. Stremplewski, M. Wojtkowski, T. S. Kern, and K. Palczewski, "Image registration and averaging of low laser power two-photon fluorescence images of mouse retina," Biomed. Opt. Express **7**(7), 2671–2691 (2016).

50. A. Myronenko and X. Song, "Intensity-based image registration by minimizing residual complexity," IEEE Trans. Med. Imaging **29**(11), 1882–1891 (2010).

51. E. G. de la Cera, G. Rodríguez, L. Llorente, F. Schaeffel, and S. Marcos, "Optical aberrations in the mouse eye," Vision Res. **46**(16), 2546–2553 (2006).

52. C. Schwarz, R. Sharma, W. S. Fischer, M. Chung, G. Palczewska, K. Palczewski, D. R. Williams, and J. J. Hunter, "Safety assessment in macaques of light exposures for functional two-photon ophthalmoscopy in humans.," Biomed. Opt. Express **7**(12), 5148–5169 (2016).

53. R. D. Ferguson, Z. Zhong, D. X. Hammer, M. Mujat, A. H. Patel, C. Deng, W. Zou, and S. A. Burns, "Adaptive optics scanning laser ophthalmoscope with integrated wide-field retinal imaging and tracking.," J. Opt. Soc. Am. A. Opt. Image Sci. Vis. **27**(11), A265-77 (2010).

54. F. Helmchen and W. Denk, "Deep tissue two-photon microscopy.," Nat. Methods **2**(12), 932–940 (2005).

55. G. Palczewska, J. Boguslawski, P. Stremplewski, L. Kornaszewski, J. Zhang, Z. Dong, X.-X. Liang, E. Gratton, A. Vogel, M. Wojtkowski, and K. Palczewski, "Noninvasive two-photon optical biopsy of retinal fluorophores," Proc. Natl. Acad. Sci. **117**(36), 22532–22543 (2020).

56. J. Schallek, Y. Geng, H. Nguyen, and D. R. Williams, "Morphology and topography of retinal pericytes in the living mouse retina using in vivo adaptive optics imaging and ex vivo characterization," Invest. Ophthalmol. Vis. Sci. **54**(13), 8237–8250 (2013).

57. B. Cohen and I. Dinstein, "New maximum likelihood motion estimation schemes for noisy ultrasound images," Pattern Recognit. **35**, 455–463 (2002).

58. Z. Wang, A. C. Bovik, H. R. Sheikh, and E. P. Simoncelli, "Image quality assessment: from error visibility to structural similarity," IEEE Trans. Image

Process. **13**(4), 600–612 (2004).

59. J. Boguslawski, G. Palczewska, S. Tomczewski, J. Milkiewicz, P. Kasprzycki, D. Stachowiak, K. Komar, M. J. Marzejon, B. L. Sikorski, A. Hudzikowski, A. Głuszek, Z. Łaszczych, K. Karnowski, G. Soboń, K. Palczewski, and M. Wojtkowski, "In vivo imaging of the human eye using a 2-photon-excited fluorescence scanning laser ophthalmoscope," J. Clin. Invest. **132**(2), (2022).

60. Y. Miao, J. Song, D. Hsu, R. Ng, Y. Jian, M. V. Sarunic, M. V. Sarunic, M. V. Sarunic, M. J. Ju, and M. J. Ju, "Numerical calibration method for a multiple spectrometer-based OCT system," Biomed. Opt. Express, Vol. 13, Issue 3, pp. 1685-1701 **13**(3), 1685–1701 (2022).

61. Y. Miao, J. Song, D. Hsu, R. Ng, Y. Jian, and M. J. Ju, "Dual operation-mode multiple spectrometer-based OCT system," in *Biophotonics Congress: Biomedical Optics 2022 (Translational, Microscopy, OCT, OTS, BRAIN)* (Optica Publishing Group, 2022), p. CS2E.4.

62. D. Schweitzer, M. Hammer, F. Schweitzer, R. Anders, T. Doebbecke, S. Schenke, E. R. Gaillard, and E. R. Gaillard, "In vivo measurement of time-resolved autofluorescence at the human fundus.," J. Biomed. Opt. **9**(6), 1214–1222 (2004).

63. C. Dysli, M. Dysli, V. Enzmann, S. Wolf, and M. S. Zinkernagel, "Fluorescence Lifetime Imaging of the Ocular Fundus in Mice," Invest. Ophthalmol. Vis. Sci. **55**(11), 7206–7215 (2014).

64. Y. Miura, "Two-Photon Microscopy (TPM) and Fluorescence Lifetime Imaging Microscopy (FLIM) of Retinal Pigment Epithelium (RPE) of Mice In Vivo.," Methods Mol. Biol. **1753**, 73–88 (2018).